Applied Mathematical Biosystems, Volume 1, Issue 1, (Jul-Dec 2025), 55-69

Applied Mathematical Biosystems

journal homepage: https://ambjournal.com

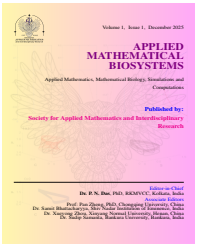

# Machine Learning-Assisted Heat and Mass Transfer Analysis in Orthotropic Piezoelectric Thermoelastic Half-Space Under Elliptic Motion Using Green–Naghdi III and Three-Phase-Lag Models

**Nikhil Chand**[1]

[1]*Ramakrishna Mission Vivekananda Centenary College, Rahara, Kolkata, West Bengal, India*

## Abstract

This study develops a computational framework for Rayleigh-type surface wave propagation in an orthotropic piezoelectric thermoelastic half-space, emphasising thermoelastic coupling, heat transfer effects, and the influence of electrical and thermal boundary conditions. Generalised thermoelastic models based on the Green–Naghdi type III (GN-III) and three-phase-lag (TPL) theories are employed to overcome the limitations of Fourier heat conduction, and secular relations for the phase velocity, attenuation, and energy dissipation are derived. Analytical simulations are carried out in MATLAB, while machine-learning surrogates in Python enable fast prediction and boundary classification. A regression-based model accurately predicts wave characteristics with reduced computation time, and a confusion-matrix classifier effectively identifies boundary states. Results show that phase velocity increases with propagation angle and saturates with wave number, while attenuation and specific loss are strongly boundary-dependent. The work is limited to homogeneous half-spaces with idealised interfaces, suggesting scope for multiscale modelling and experimental validation. The integrated GN-III/TPL and ML-assisted framework offers a powerful tool for thermoelastic wave analysis with potential applications in surface acoustic wave sensing, non-destructive testing, aerospace structures, and energy harvesting systems.

**Keywords:** *Orthotropic piezoelectric thermoelasticity; Three-phase-lag theory; Green–Naghdi III model; Machine learning; Elliptic Motion.*

**Corresponding author:** Nikhil Chand *E-mail address:* nikhilchand003@gmail.com
**Received:** Novmber 11, 2025 **Revised:** December 27, 2025 **Accepted:** December 29, 2025 **Published:** December 30, 2025


## 1. Introduction

The classical thermoelasticity theory based on Fourier's heat conduction law leads to a parabolic heat equation, which implies an unrealistic infinite speed of thermal signal propagation. This limitation becomes particularly evident in low-temperature environments and under high heat flux conditions, where finite thermal response times are physically observed. To address this inconsistency, several generalized thermoelastic theories have been proposed by introducing hyperbolic-type heat conduction equations. In these models, thermal disturbances propagate in the form of waves with finite velocity, commonly referred to as second sound. As a result, generalized thermoelasticity has emerged as an effective framework for describing thermo-mechanical interactions in modern engineering and technological applications.

Wave propagation in Orthotropic piezoelectric solids has attracted sustained research interest due to its importance in both theoretical mechanics and applied sciences. Surface acoustic waves, especially Rayleigh-type waves, are of particular significance because of their confinement near free surfaces and their strong sensitivity to boundary conditions and material anisotropy. These properties are extensively utilized in the development of acoustic sensors, microelectromechanical systems (MEMS), and nondestructive testing techniques [1–5]. Earlier investigations on Orthotropic piezoelectric substrates have enhanced the understanding of electromechanical coupling, thermal influences, and defect-related effects, thereby providing useful guidance for improving device efficiency and operational reliability [6–9].

To overcome the shortcomings of classical coupled and uncoupled thermoelastic models, several generalized theories have been formulated. The Green–Naghdi type III (GN-III) theory incorporates finite thermal wave speed without energy dissipation, whereas the three-phase-lag (TPL) theory introduces separate delay times associated with heat flux and temperature gradient to represent micro-scale thermal relaxation more accurately [10–14]. These generalized approaches are particularly suitable for

high-frequency applications and materials with microstructural effects, where classical Fourier-based descriptions fail. Previous studies have demonstrated that surface wave propagation in such generalized thermoelastic media is highly sensitive to boundary conditions and material parameters [15–19].

In Orthotropic piezoelectric media, the application of GN-III and TPL theories has revealed notable changes in dispersion characteristics, attenuation behavior, and stress distributions of propagating waves [20–23]. These findings are especially relevant for commonly used Orthotropic piezoelectric materials such as $LiNbO_3$ and PZT, which are widely employed in sensing, actuation, and energy harvesting technologies. Additionally, imperfections such as voids, defects, and non-ideal interfaces further influence wave propagation, emphasizing the need for comprehensive analytical models capable of addressing realistic boundary conditions [24–27]. Such models are essential for both advancing theoretical understanding and supporting practical applications in electronics, aerospace engineering, and biomedical ultrasonics.

While analytical formulations provide fundamental physical insights, solving the resulting dispersion relations over wide parameter ranges can be computationally demanding. In this regard, machine learning (ML) offers a useful complementary approach by acting as a surrogate model trained on analytically generated datasets. Regression-based ML techniques enable rapid prediction of phase velocity, attenuation, and specific loss, whereas classification models can effectively identify electrical and thermal boundary conditions from wave response data. This combined analytical–ML framework significantly reduces computational effort and supports efficient parametric analysis and intelligent design of piezoelectric devices [28–39].

In this work, Rayleigh-type surface wave propagation in a Orthotropic piezoelectric half-space is examined under different electrical and thermal boundary conditions within the frameworks of GN-III and TPL theories. The analytical solutions are further complemented by machine learning-based predictions and boundary condition classification, resulting in an integrated approach that bridges classical mechanics, computational modeling, and data-driven intelligence.

## 2. Mathematical formulation of the model I and II

The governing equations and constitutive relations for a linear Orthotropic-piezothermoelastic, homogeneous medium are:

(A) Strain-displacement relation:

$$\varepsilon_{ij} = \frac{1}{2}\left(u_{i,j} + u_{j,i}\right). \tag{1}$$

(B) Stress-strain-temperature and electric field relations:

$$\sigma_{ij} = C_{ijkl}\varepsilon_{kl} - e_{kij}E_k - \beta_{ij}\theta. \tag{2}$$

(C) Equations of motion without body force:

$$\sigma_{ij,j} = \rho\ddot{u}_i. \tag{3}$$

(D) Gauss equation:

$$D_{i,i} = 0, \quad D_i = e_{ijk}\varepsilon_{jk} + \epsilon_{ij}E_j + p_i\theta. \tag{4}$$

(E) Law of conservation of energy:

$$q_{i,i} = -\rho\dot{\eta}\theta_0. \tag{5}$$

(F) Entropy equation:

$$\rho\eta = \frac{\rho C_e}{\theta_0}\theta + \beta_{ij}\varepsilon_{ij} + p_i E_i. \tag{6}$$

(G) Heat conduction equation: Three phase lag thermoelastic model [7]:

$$\left(1 + \tau_q\frac{\partial}{\partial t} + \frac{\tau_q^2}{2}\frac{\partial^2}{\partial t^2}\right)\dot{q}_i = -\Upsilon^*_{ij}\left(1 + \tau_\nu\frac{\partial}{\partial t}\right)\theta_{,j} - \Upsilon_{ij}\left(1 + \tau_\theta\frac{\partial}{\partial t}\right)\dot{\theta}_{,j}. \tag{7}$$

Green-Naghdi type III (GN-III) thermoelastic model with dual phase [15]:

$$\left(1 + \tau_q\frac{\partial}{\partial t}\right)\dot{q}_i = -\Upsilon^*_{ij}\left(1 + \tau_\nu\frac{\partial}{\partial t}\right)\theta_{,j} - \Upsilon_{ij}\dot{\theta}_{,j}. \tag{8}$$

Here, $\dot{\nu} = \theta$. Equation (8) can be recovered from equation (7) by taking $\tau_\theta = 0$ and considering only first order partial derivatives. In equations (1)-(8) $i, j, k, l = 1, 2, 3$, $\rho$ is the mass density, $\varepsilon_{ij}\left(=\varepsilon_{ji}\right)$ is the strain tensor, $\sigma_{ij}\left(=\sigma_{ji}\right)$ is the stress tensor, $C_{ijkl}$ denotes the symmetric elastic tensor; $e_{kij}$ piezoelectric moduli tensor is symmetric with respect to $i, j$; $\beta_{ij}$ is non-singular and denotes the thermal elastic coupling tensor. $\theta$ is the temperature change of the material, $\theta_0$ is the reference uniform temperature, $u_i$ is mechanical displacement, $C_e$ is the specific heat at constant strain and $p_i$ is the pyroelectric moduli, $\epsilon_{ij}$ is electric permittivity; $q_i$ is the heat flux vector. $\Upsilon^*_{ij}\left(=\Upsilon^*_{ji}\right)$, $\Upsilon_{ij}\left(=\Upsilon_{ji}\right)$ are heat conductivity rate and coefficient of heat conduction of the material, both are positive definite, $\eta$ is the entropy and $\tau_q; \tau_\nu; \tau_\theta$ is an intrinsic thermal properties of the material termed as phase-lag of the heat flux; phase-lag of the thermal displacement gradient; phase-lag of the temperature gradient respectively, which satisfies the inequality $0 \le \tau_\nu < \tau_\theta < \tau_q$. Also, $E_i = -\varphi_{,i}$, where $E_i$ is the electric field and $\varphi$ is the electric potential function. Here $D_i$ represents electric displacements. $\dot{()}$ denotes time derivative and $()_{,j}$ indicates partial derivatives with respect to $x_j$ unless and otherwise stated.

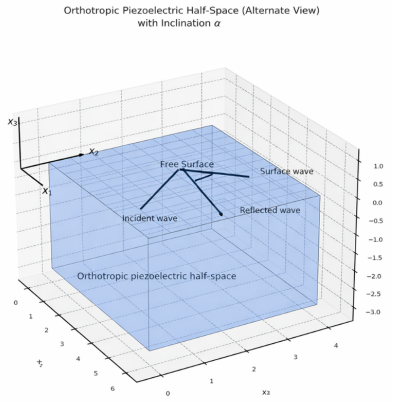


**Figure 1.** 3D schematic of an orthotropic piezothermoelastic half-space with free surface at $x_3 = 0$. An oblique wave impinges on the surface, producing a reflected bulk wave and a surface-guided wave. The inclination angle $\alpha$ is measured in the surface plane between the $x_1$-axis and the propagation direction. Coordinate axes $x_1, x_2, x_3$ follow the adopted system.

### 2.1. Description of the model I

For the present study a homogeneous, orthotropic, thermally and electrically conducting ortho-piezo-thermoelastic half-space with initial temperature $\theta_0$ in undisturbed state assumed such

that $\left|\frac{\theta}{\theta_0}\right| << 1$ and initial electric potential $\varphi_0$ is considered (See the schamatic diagram for this model in Fig.1). Cartesian co-ordinate system ($x_1$, $x_2$, $x_3$) is introduced in such a manner that the origin of the co-ordinate system lies at any point on the horizontal surface, the axis of material symmetry, $x_3$−axis, indicating vertically downwards into the half-space, denoted by $x_3 \geqslant 0$ .

From (2), it yields

$$\left.\begin{array}{c} \sigma_{11} = C_{11}\varepsilon_{11} + C_{12}\varepsilon_{22} + C_{13}\varepsilon_{33} - e_{31}E_3 - \beta_{11}\theta, \\ \sigma_{13} = 2C_{55}\varepsilon_{13} - e_{15}E_1, \\ \sigma_{33} = C_{13}\varepsilon_{11} + C_{23}\varepsilon_{22} + C_{33}\varepsilon_{33} - e_{33}E_3 - \beta_{33}\theta, \\ D_1 = 2e_{15}\varepsilon_{13} + \epsilon_{11}E_1, \\ D_3 = e_{31}\varepsilon_{11} + e_{32}\varepsilon_{22} + e_{33}\varepsilon_{33} + \epsilon_{33}E_3 + p_3\theta. \end{array}\right\} . \quad (9)$$

In the view of equation (9), the basic governing equations (3) and (5)-(8), can be postulated as without body forces, heat sources and charge density:

$$C_{11}u_{1,11} + C_{13}u_{3,13} + C_{55}(u_{1,33} + u_{3,13}) + (e_{15} + e_{31})\varphi_{,13} - \beta_{11}\theta_{,1} = \rho\ddot{u}_1. \quad (10)$$

$$C_{55}(u_{1,13} + u_{3,11}) + C_{13}u_{1,13} + C_{33}u_{3,33} + e_{15}\varphi_{,11} + e_{33}\varphi_{,33} - \beta_{33}\theta_{,3} = \rho\ddot{u}_3. \quad (11)$$

$$e_{15}(u_{1,13} + u_{3,11}) + e_{31}u_{1,13} + e_{33}u_{3,33} - \epsilon_{11}\varphi_{,11} - \epsilon_{33}\varphi_{,33} + p_3\theta_{,3} = 0. \quad (12)$$

$$\Upsilon^*_{11}\left(1 + \tau_\nu\frac{\partial}{\partial t}\right)\theta_{,11} + \Upsilon^*_{33}\left(1 + \tau_\nu\frac{\partial}{\partial t}\right)\theta_{,33} + \Upsilon_{11}\left(1 + \tau_\theta\frac{\partial}{\partial t}\right)\dot{\theta}_{,11} + \Upsilon_{33}\left(1 + \tau_\theta\frac{\partial}{\partial t}\right)\dot{\theta}_{,33} = \left(1 + \tau_q\frac{\partial}{\partial t} + \frac{\tau_q^2}{2}\frac{\partial^2}{\partial t^2}\right)\left[\rho C_e\ddot{\theta} + \theta_0\left(\beta_{11}\ddot{u}_{1,1} + \beta_{33}\ddot{u}_{3,3} - p_3\ddot{\varphi}_{,3}\right)\right]. \quad (13)$$

where $\beta_{11} = \left(C_{11} + C_{12)}\right)\vartheta_1 + C_{13}\vartheta_3$, $\beta_{33} = 2C_{13}\vartheta_1 + C_{33}\vartheta_3$; and $\vartheta_1$, $\vartheta_3$ are, respectively, the coefficient of thermal expansions.

For convenience, following dimensionless quantities are defined and used for further calculations:

$$\left.\begin{array}{c} x_i' = \frac{\omega^* x_i}{\upsilon_p},\ u_i' = \frac{\rho\omega^*\upsilon_p u_i}{\beta_{11}\theta_0},\ \upsilon_p = \sqrt{\frac{C_{11}}{\rho}},\ \omega^* = \frac{C_e C_{11}}{\Upsilon_{11}}, \\ t' = \omega^* t,\ \theta' = \frac{\theta}{\theta_0}, C_1 = \frac{C_{33}}{C_{11}},\ C_2 = \frac{C_{55}}{C_{11}},\ C_3 = \frac{C_{13}+C_{55}}{C_{11}}, \\ C_4 = \frac{C_{11}-C_{12}}{2C_{11}},\ e_1 = \frac{e_{15}+e_{31}}{e_{33}},\ e_2 = \frac{e_{15}}{e_{33}},\ \bar{\epsilon} = \frac{\epsilon_{11}}{\epsilon_{33}}, \\ \epsilon_p = \frac{\omega^* e_{33}\varphi_0}{\upsilon_p\beta_1\theta_0},\ \epsilon_n = \eta_3\epsilon_p,\ \eta_3 = \frac{\epsilon_{33}C_{11}}{e_{33}^2},\ \epsilon = \frac{\theta_0\beta_1^2}{\rho C_e C_{11}}, \\ \overline{\Upsilon} = \frac{\Upsilon_{33}}{\Upsilon_{11}},\ \overline{\beta} = \frac{\beta_{33}}{\beta_{11}},\ \sigma_{ij}' = \frac{\sigma_{ij}}{\beta_{11}\theta_0},\ D_i' = \frac{D_i C_{11}}{\beta_{11}\theta_0 e_{33}}, \\ d' = \frac{\omega^* d}{\upsilon_p},\ h' = \frac{h\upsilon_p}{\omega^*},\ \varphi' = \frac{\varphi}{\varphi_0},\ \xi' = \frac{\xi\upsilon_p}{\omega^*},\ \omega' = \frac{\omega}{\omega^*}, c' = \\ \frac{c}{\upsilon_p},\ \varphi' = \frac{\varphi}{\varphi_0},\ p = \frac{p_3 C_{11}}{\beta_{11}e_{33}},\ \left(\tau_q', \tau_\nu', \tau_\theta'\right) = \omega^*\left(\tau_q, \tau_\nu, \tau_\theta\right). \end{array}\right\} \quad (14)$$

Here $\upsilon_p$ is the longitudinal wave velocity in the half-space, $\omega^*$ represents the characteristic frequency of the half-space, $\epsilon_p$ and $\epsilon$ are, respectively, the piezoelectric coupling and thermo-elastic coupling parameter.

With the view of the equation (14) in equations (10) - (13) and suppressing primes for convenience, it yields the following equations:

$$\left.\begin{array}{c} u_{1,11} + C_2u_{1,33} + C_3u_{3,13} + e_1\epsilon_p\varphi_{,13} - \theta_{,1} = \ddot{u}_1, \\ C_3u_{1,13} + C_2u_{3,11} + C_1u_{3,33} + \varepsilon_p\left(e_2\varphi_{,11} + \varphi_{,33}\right) - \overline{\beta}\dot{\theta} = \ddot{u}_3, \\ e_1u_{1,13} + e_2u_{3,11} + u_{3,33} - \epsilon_n\left(\bar{\epsilon}\varphi_{,11} + \varphi_{,33}\right) + p\theta_{,3} = 0, \\ \left(1 + \tau_\theta\frac{\partial}{\partial t}\right)\dot{\theta}_{,11} + \overline{\Upsilon}\left(1 + \tau_\theta\frac{\partial}{\partial t}\right)\dot{\theta}_{,33} + \Upsilon_1\left(1 + \tau_\nu\frac{\partial}{\partial t}\right)\theta_{,11} + \Upsilon_3\left(1 + \tau_\nu\frac{\partial}{\partial t}\right)\theta_{,33} \\ -\left(1 + \tau_q\frac{\partial}{\partial t} + \frac{\tau_q^2}{2}\frac{\partial^2}{\partial t^2}\right)\ddot{\theta} = \left(1 + \tau_q\frac{\partial}{\partial t} + \frac{\tau_q^2}{2}\frac{\partial^2}{\partial t^2}\right)[\epsilon\left(\ddot{u}_{1,1} + \bar{\beta}\ddot{u}_{3,3} - \epsilon_p p\ddot{\varphi}_{,3}\right)], \end{array}\right\} \quad (15)$$

where $\Upsilon_1 = \frac{\Upsilon^*_{11}\omega^*}{\Upsilon_{11}}$, $\Upsilon_3 = \frac{\Upsilon^*_{33}\omega^*}{\Upsilon_{11}}$.

Again using equation (14) in equation (9), the dimensionless form of stresses and electrical displacement components in $x_1 - x_3$ plane can be written as (suppressing primes for convenience)

$$\left.\begin{array}{c} \sigma_{11} = u_{1,1} + (C_3 - C_2)u_{3,3} + \epsilon_p(e_1 - e_2)\varphi_{,3} - \theta, \\ \sigma_{13} = C_2\left(u_{3,1} + u_{1,3}\right) + e_2\epsilon_p\varphi_{,1}, \\ \sigma_{33} = (C_3 - C_2)u_{1,1} + C_1u_{3,3} - \overline{\beta}\theta + \epsilon_p\varphi_{,3}, \\ D_1 = e_2\left(u_{1,3} + u_{3,1}\right) - \bar{\epsilon}\epsilon_n\varphi_{,1}, \\ D_3 = (e_1 - e_2)u_{1,1} + u_{3,3} - \epsilon_n\varphi_{,3} + p\theta. \end{array}\right\} \quad (16)$$

### 2.2. Brief Mathematics for Model II

**Constitutive relations for Model II [21]:**

$$\begin{aligned} \left(1 - \xi^2\nabla^2\right)\sigma_{ij} &= \sigma_{ij}^L = c_{ijkl}e_{kl}(\bar{\xi}) - \eta_{ij}E_k(\bar{\xi}) - \beta_{ij}^T\theta(\bar{\xi}) + \gamma_{ij}\psi(\bar{\xi}), & \text{(a)} \\ \left(1 - \xi^2\nabla^2\right)\sigma_i^1 &= \left(\sigma_i^1\right)^L = A_{ij}\psi_{,j}(\bar{\xi}) + h_{ij}E_j(\bar{\xi}), & \text{(b)} \\ \left(1 - \xi^2\nabla^2\right)\zeta &= \zeta^L = -\gamma_{ij}e_{ij}(\bar{\xi}) - g_kE_k(\bar{\xi}) - a\psi(\bar{\xi}) + \nu\theta(\bar{\xi}), & \text{(c)} \\ \left(1 - \xi^2\nabla^2\right)D_i &= D_i^L = \eta_{ijk}e_{jk}(\bar{\xi}) + \varepsilon_{ij}E_j(\bar{\xi}) + \tau_i\theta(\bar{\xi}) - g_i\psi(\bar{\xi}) - h_{ij}\psi_{,j}(\bar{\xi}), & \text{(d)} \\ \left(1 - \xi^2\nabla^2\right)\rho S^* &= \left(\rho S^*\right)^L = \beta_{ij}^Te_{ij}(\bar{\xi}) + \tau_iE_i(\bar{\xi}) + \nu\psi(\bar{\xi}) + \frac{\rho C_E\theta(\bar{\xi})}{\theta_0}. & \text{(e)} \end{aligned}$$

**Equations of motion of Model II [21]:**

$$\sigma_{ij,j}^L + \left(1 - \xi^2\nabla^2\right)F_i = \rho\left(1 - \xi^2\nabla^2\right)\ddot{u}_i, \quad \text{(f)}$$

$$D_{i,i} = 0, \qquad \text{where } E_i = -\phi_{,i}, \quad \text{(g)}$$

$$\left(\sigma_{i,i}^1\right)^L + \zeta^L + \rho\left(1 - \varepsilon^2\nabla^2\right)l_1^* = \chi\left(1 - \varepsilon^2\nabla^2\right)\ddot{\psi}. \quad \text{(h)}$$

### 2.3. Boundary Conditions

At the free surface ($z = 0$) of the considered nonlocal orthotropic piezothermoelastic substrate, we introduce the following specific boundary conditions.

*Mechanical conditions:*

$$\sigma_{xz} = 0, \qquad \sigma_{zz} = 0, \quad \text{(i)}$$

*Equilibrated stress condition:*

$$\sigma_z^1 = 0, \quad \text{(j)}$$

*Dielectrical displacement condition:*

$$D_z = 0, \quad \text{(k)}$$

*Thermal condition:*

$$\theta = 0. \quad \text{(l)}$$

### Path of the Surface Particles

The components of mechanical displacement in the present investigation are formulated as [21]

$$(u, w) = \sum_{m=1}^{5}(1, P_m)\,\tilde{u}_m\exp[i\omega(qx + s_mz - t)]. \quad \text{(m)}$$

For a given real value of $q$, the actual displacements obtained may be expressed in the following form [21]

$$(U, W) = \Re(u, w) \approx \Re\left(\sum_{m=1}^{5}(1, P_m)\exp[i\omega(qx + s_m z - t)]\right). \tag{n}$$

## 3. Boundary conditions Model I

The preceding governing equations can be solved by using the below mentioned mechanical, electrical, and thermal boundary conditions.

### 3.1. Mechanical boundary conditions

The surface of the half-space is supposed to be stress free so

$$\sigma_{13} = 0, \qquad \sigma_{33} = 0. \tag{17}$$

### 3.2. Electrical boundary conditions

The surface of the half-space is assumed to be either electrically shorted or open which mathematically yields the following electrical boundary conditions

$$\varphi = 0, \qquad D_3 = 0. \tag{18}$$

### 3.3. Thermal boundary conditions

Thermal boundary conditions can be elicited as

$$\theta_{,3} + \Omega\theta = 0, \tag{19}$$

here $\Omega$ is the coefficient of surface heat transfer and $\Omega \to 0$ give rises to thermally insulated condition whereas $\Omega \to \infty$ leads to isothermal boundary condition.

## 4. Solution procedure

The solution of the considered equations (15) can be decomposed in terms of normal modes in the following form

$$(u_1, u_3, \varphi, \theta) = (1, V, W, T)\, U\, \exp\{i\xi\,(x_1 \sin\alpha + mx_3 - ct)\}, \tag{20}$$

where $\xi$, $c$, $\omega$ denotes, respectively, the dimensionless wave number, phase velocity and angular frequency of the waves. Also $c = \frac{\omega}{\xi}$, $\alpha$ represents the inclination angle of the wave normal to the axis of symmetry ($x_3$−axis) and $m$ is an unknown parameter which defines the penetration depth of the wave. $V$, $W$, $T$ are the amplitude ratios of the mechanical displacement $u_3$, electrical potential $\varphi$ and temperature change $\theta$ to that of mechanical displacement $u_1$ respectively. Inserting (20) in (15) generates a system of homogeneous linear equations in terms of amplitudes, $\boldsymbol{\Gamma_{ij}X} = \mathbf{0}$ , i.e,

$$\begin{bmatrix} a_{11} & C_3ms & \epsilon_p e_1 ms & -\frac{s}{i\xi} \\ C_3ms & a_{22} & \epsilon_p a_{23} & -\frac{\tilde{\beta}}{i\xi} \\ e_1 ms & a_{23} & -\epsilon_n\left(\bar{\epsilon}s^2 + m^2\right) & \frac{pm}{i\xi} \\ A_3\epsilon c^2 s & \epsilon\tilde{\beta}mc^2 & \epsilon p\epsilon_p c^2 m & \frac{a_{44}}{i\xi} \end{bmatrix} \begin{bmatrix} 1 \\ V \\ W \\ T \end{bmatrix} = \begin{bmatrix} 0 \\ 0 \\ 0 \\ 0 \end{bmatrix}, \tag{21}$$

where $a_{11} = s^2 + C_2m^2 - c^2$, $a_{22} = C_2s^2 + C_1m^2 - c^2$, $a_{23} = e_2s^2 + m^2$, $a_{44} = -A_3c^2 + i\xi\left(\widetilde{A}s^2 + \widetilde{B}m^2\right)$, $s = \sin\alpha, A_1 = (1 + \tau_\theta(-ic\xi))$, $A_2 = (1 + \tau_\nu(-ic\xi))$, $A_3 = \left(1 + \tau_q(-ic\xi) + \frac{\tau_q^2}{2}(-c^2\xi^2)\right)$, $\widetilde{A} = \left(A_1c + \frac{\Upsilon_1 A_2}{i\xi}\right)$and $\widetilde{B} = \left(-\bar{\Upsilon}A_1c - \frac{\Upsilon_3 A_2}{i\xi}\right)$.

The non-trivial solution of the equation (21) is ensured when the determinant of the coefficient matrix vanishes, i.e., $\left|\boldsymbol{\Gamma_{ij}}\right| = 0$ which constitutes

$$\begin{vmatrix} a_{11} & C_3ms & \epsilon_p e_1 ms & -s \\ C_3ms & a_{22} & \epsilon_p a_{23} & -\tilde{\beta} \\ e_1 ms & a_{23} & -\epsilon_n\left(\bar{\epsilon}s^2 + m^2\right) & pm \\ A_3\epsilon c^2 s & \epsilon\tilde{\beta}mc^2 & \epsilon p\epsilon_p c^2 m & a_{44} \end{vmatrix} = 0. \tag{22}$$

Expanding the determinant, the following polynomial equation in $m$ is obtained

$$m^8 + A_1m^6 + A_2m^4 + A_3m^2 + A_4 = 0. \tag{23}$$

The expressions for $A_i (i = 1, 2, 3, 4)$ are available in Appendix A.

The characteristic equation (23) being bi-quadratic in $m^2$so gives four characteristic roots for $m_i^2$, $(i = 1, 2, 3, 4)$. Here the major concern is with the surface waves whose motion is confined to the free surface of the half-space, hence the characteristic roots must satisfy the radiation condition, i.e, $Im(m_i) \geq 0$. So the bounded solution for mechanical displacement, electrical potential and temperature change can be expressed as

$$(u_1, u_3, \varphi, \theta) = \sum_{n=1}^{4}(1, V_n, W_n, T_n)\, U_n \exp[i\xi\alpha_n], \tag{24}$$

where, $\alpha_n = x_1 \sin\alpha + m_n x_3 - ct$, for every $m_n$, $(n = 1, 2, 3, 4)$ the amplitude ratios can be stated as,

$$V_n = \frac{\Gamma_{42}(m_n)}{\Gamma_{41}(m_n)},\ W_n = \frac{\Gamma_{43}(m_n)}{\Gamma_{41}(m_n)},\ T_n = \frac{\Gamma_{44}(m_n)}{\Gamma_{41}(m_n)}, \tag{25}$$

where $\Gamma_{4j}(m_n)$, $j = 1, 2, 3, 4$ indicates the co-factor of the element $\Gamma_{4j}$ corresponding to the root $m_n$, $n = 1, 2, 3, 4$. The values of $\Gamma_{4j}(m_n), j = 1, 2, 3, 4$ are provided in Appendix A.

Substituting equation (24) on equation (16), the expressions for stresses, electrical displacement, and temperature gradient are as follows:

$$(\sigma_{13}, \sigma_{33}, D_3, \theta_{,3}) = \sum_{n=1}^{4} i\xi\,(B_{1n}, B_{2n}, B_{3n}, m_n T_n)\, U_n e^{i\xi\alpha_n}, \tag{26}$$

where $B_{1n}$, $B_{2n}, B_{3n}$ are defined in Appendix A.

## 5. Derivation of secular equations

### 5.1. Stress free, electrically open and thermally insulated surface of the half-space

From the boundary conditions (17), (18), and (19) at the free surface, at $x_3 = 0$, the following system of four homogeneous linear simultaneous equations in amplitude $U_n$, $n = 1, 2, 3, 4$ are obtained

$$\sum_{n=1}^{4} B_{1n}U_n = 0, \qquad \sum_{n=1}^{4} B_{2n}U_n = 0,$$
$$\sum_{n=1}^{4} B_{3n}U_n = 0, \qquad \sum_{n=1}^{4} m_n T_n U_n = 0.$$

which can be penned in terms of matrix notation as $\boldsymbol{\Gamma_{B1}\Gamma_U} = \mathbf{0}$. Here $\boldsymbol{\Gamma_{B1}}$denotes fourth order square matrix provided in Appendix

B and $\boldsymbol{\Gamma_U} = [U_1, U_2, U_3, U_4]^\top$. Here $[]^\top$ denotes the transpose of the matrix []. For the existence of non-trivial solution of the above simultaneous equations is $|\boldsymbol{\Gamma_{B1}}| = 0$, which after algebraic computation reduces to

$$m_1T_1\Gamma_1 + m_2T_2\Gamma_2 + m_3T_3\Gamma_3 + m_4T_4\Gamma_4 = 0. \tag{27}$$

Here, $\Gamma_1 = \begin{vmatrix} B_{12} & B_{13} & B_{14} \\ B_{22} & B_{23} & B_{24} \\ B_{32} & B_{33} & B_{34} \end{vmatrix}$, $\Gamma_2 = \begin{vmatrix} B_{11} & B_{13} & B_{14} \\ B_{21} & B_{23} & B_{24} \\ B_{31} & B_{33} & B_{34} \end{vmatrix}$,

$\Gamma_3 = \begin{vmatrix} B_{11} & B_{12} & B_{14} \\ B_{21} & B_{22} & B_{24} \\ B_{31} & B_{32} & B_{34} \end{vmatrix}$, $\Gamma_4 = \begin{vmatrix} B_{11} & B_{12} & B_{13} \\ B_{21} & B_{22} & B_{23} \\ B_{31} & B_{32} & B_{33} \end{vmatrix}$.

The equation (27) is the secular equation for propagation of surface waves under stress free, electrically open and thermally insulated boundaries of ortho-piezo-thermoelastic half-space.

### 5.2. Stress free, electrically open and isothermal surface of the half-space

Invoking the boundary conditions (17), (18), and (19) at the free surface $x_3 = 0$, the following system of four homogeneous linear simultaneous equations in amplitude $U_n$, $n = 1, 2, 3, 4$ are as follows

$$\sum_{n=1}^{4} B_{1n}U_n = 0, \quad \sum_{n=1}^{4} B_{2n}U_n = 0,$$
$$\sum_{n=1}^{4} B_{3n}U_n = 0, \quad \sum_{n=1}^{4} T_nU_n = 0.$$

which can be expressed as $\boldsymbol{\Gamma_{B2}\Gamma_U} = \mathbf{0}$. Here $\boldsymbol{\Gamma_{B2}}$ is a square matrix of order 4 given in Appendix B. The non-trivial solution of the above system of equations exists when $|\boldsymbol{\Gamma_{B2}}|$ vanishes, which after mathematical calculation can be written as

$$T_1\Gamma_1 + T_2\Gamma_2 + T_3\Gamma_3 + T_4\Gamma_4 = 0, \tag{28}$$

which is the secular equation for propagation of surface waves under stress free, electrically open and isothermal boundaries of ortho-piezo-thermoelastic half-space.

### 5.3. Stress free, electrically shorted and thermally insulated surface of the half-space

Applying the boundary conditions equations (17), (18), and (19) at the free surface $x_3 = 0$, the following system of four homogeneous linear simultaneous equations in amplitude $U_n$, $n = 1, 2, 3, 4$ are obtained

$$\sum_{n=1}^{4} B_{1n}U_n = 0, \quad \sum_{n=1}^{4} B_{2n}U_n = 0,$$
$$\sum_{n=1}^{4} W_nU_n = 0, \quad \sum_{n=1}^{4} m_nT_nU_n = 0.$$

which can be formulated as $\boldsymbol{\Gamma_{B3}\Gamma_U} = \mathbf{0}$. Here $\boldsymbol{\Gamma_{B3}}$ is a square matrix of order 4 given in Appendix B. Above system of equations hold a non-trivial solution if the determinant of $\boldsymbol{\Gamma_{B3}}$ is zero, which after algebraic computation reduces to

$$m_1T_1\Gamma_1^s + m_2T_2\Gamma_2^s + m_3T_3\Gamma_3^s + m_4T_4\Gamma_4^s = 0. \tag{29}$$

$\Gamma_i^s$ can be acquired by replacing the third row of $\Gamma_i$ by $W_i$, $i = 1, 2, 3, 4$ so that

$\Gamma_1^s = \begin{vmatrix} B_{12} & B_{13} & B_{14} \\ B_{22} & B_{23} & B_{24} \\ W_2 & W_3 & W_4 \end{vmatrix}$, $\Gamma_2^s = \begin{vmatrix} B_{11} & B_{13} & B_{14} \\ B_{21} & B_{23} & B_{24} \\ W_1 & W_3 & W_4 \end{vmatrix}$,

$\Gamma_3^s = \begin{vmatrix} B_{11} & B_{12} & B_{14} \\ B_{21} & B_{22} & B_{24} \\ W_1 & W_2 & W_4 \end{vmatrix}$, $\Gamma_4^s = \begin{vmatrix} B_{11} & B_{12} & B_{13} \\ B_{21} & B_{22} & B_{23} \\ W_1 & W_2 & W_3 \end{vmatrix}$.

Here the equation (29) is the secular equation for propagation of surface waves under stress free, electrically shorted and thermally insulated boundaries of ortho-piezo-thermoelastic half-space.

### 5.4. Stress free, electrically shorted and isothermal surface of the half-space

Implementing the boundary conditions equations (17), (18), and (19) at the free surface $x_3 = 0$, the following system of four homogeneous linear simultaneous equations in amplitude $U_n$, $n = 1, 2, 3, 4$ are obtained

$$\sum_{n=1}^{4} B_{1n}U_n = 0, \quad \sum_{n=1}^{4} B_{2n}U_n = 0,$$
$$\sum_{n=1}^{4} W_nU_n = 0, \quad \sum_{n=1}^{4} T_nU_n = 0.$$

Proceeding as above, the equation yields as

$$T_1\Gamma_1^s + T_2\Gamma_2^s + T_3\Gamma_3^s + T_4\Gamma_4^s = 0. \tag{30}$$

Equation (30) gives the secular equation for propagation of surface waves under stress free, electrically shorted and isothermal boundaries of ortho-piezo-thermoelastic half-space. Equations (27)-(30) utters a relation between phase velocity, wave number, and attenuation coefficient of surface waves in a stress free, electrically open or shorted and thermally isolated or isothermal boundaries of ortho-piezo-thermoelastic half-space. These wave numbers and also phase velocities are complex quantities which are attenuated in space. Since the characteristic equation (23) and secular equations (27)-(30) are complex equations, hence provides complex values of $c$. Generally to solve these equations the following relation is considered

$$\frac{1}{c} = \frac{1}{V} + \frac{i\varrho}{\omega}, \tag{31}$$

so that $\xi = \chi + i\varrho$, where $\chi = \frac{\omega}{V}$, $V$ and $\varrho$ are real numbers. Here $V' = \frac{V}{v_p}$ and $\varrho' = v_p\varrho$ are dimensionless phase speed and attenuation coefficient respectively. Primes are suppressed for convenience. Let the roots of the equation (23) be of the form $m_n = \lambda_n + i\mu_n$, then the solution of the plane wave equation (24) reduces to

$$(u_1, u_3, \varphi, \theta) = \sum_{n=1}^{4} (1, V_n, W_n, T_n)\, U_n \exp[-\kappa_m - i\kappa_n], \tag{32}$$

where $\kappa_m = \varrho \sin\alpha\, x_1 + k_n^I x_3$, $\kappa_n = k_n^R x_3 + \chi(x_1 \sin\alpha - Vt)$, $k_n^R = \chi m_n^R$, $k_n^I = \chi m_n^I$, $m_n^R = \lambda_n - \frac{\mu_n\varrho}{\chi}$, and $m_n^I = \mu_n\lambda_n - \frac{\lambda_n\varrho}{\chi}$.

## 6. Expression for phase velocity, attenuation coefficient and specific loss

From the above analytical results derived in the preceding section, the behaviour of the waves can be determined by the characteristics of wave field such as phase velocity, attenuation coefficient and specific loss in view of the following formulae:

**Phase velocity:** Phase velocity is given by, Phase velocity $= \frac{\omega}{Re(\xi)} = \frac{\omega}{\chi}$.

**Attenuation coefficient:** Attenuation coefficient can be defined as, Attenuation coefficient $= Im(\xi) = \varrho$, where $\xi$ is a complex quantity and $Re(\xi)$ and $Im(\xi)$ indicates, respectively, the real and imaginary part of the complex number $\xi$.

**Specific loss:** Specific loss defines the internal friction of a material [40]. The definition of specific loss is the ratio of energy $(\Delta\Omega)$ dissipated in a sample through a stress cycle to the elastic energy $(\Omega)$ stored in that particular sample when the stress is maximum. Specific loss equals to 4 times the absolute value of the imaginary part of $\xi$ to the real part of $\xi$, in the case of sinusoidal plane waves with small amplitudes [41].

Specific loss $\left(\frac{\Delta\Omega}{\Omega}\right) = 4\pi\left|\frac{Im(\xi)}{Re(\xi)}\right|$, where $\xi$ is a complex number with $Im(\xi) > 0$. So, $\frac{\Delta\Omega}{\Omega} = 4\pi\left|\frac{\varrho}{\chi}\right| = 4\pi\left|\frac{V\varrho}{\omega}\right|$.

## 7. Amplitudes of Surface displacements, temperature change and electrical potential function

In this section the expressions for amplitudes of mechanical displacements $(u_1^s, u_3^s)$, temperature change $(\varphi_s)$ and electrical potential functions $(\theta_s)$ at the free surface $x_3 = 0$ for a stress free, electrically open and thermally insulated or isothermal boundary of the half-space in the course of surface (Rayleigh type) waves propagation is obtained. Here,

$$\left.\begin{aligned} u_1^s &= U_1\Lambda\exp\{-\alpha_t\},\ u_3^s = U_3\Lambda\exp\{-\alpha_t\},\\ \theta_s &= \Psi_1\Lambda\exp\{-\alpha_t\},\ \varphi_s = \Phi_1\Lambda e\exp\{-\alpha_t\},\end{aligned}\right\} \tag{33}$$

where $\alpha_t = i\chi(x_1\sin\alpha - Vt)$, $\Lambda = \Gamma_1\exp\{-\varrho x_1\sin\alpha\}$, with

$$\left.\begin{aligned} U_1 &= \tfrac{\Gamma_1-\Gamma_2+\Gamma_3-\Gamma_4}{\Gamma_1},\ U_3 = \tfrac{V_1\Gamma_1-V_2\Gamma_2+V_3\Gamma_3-V_4\Gamma_4}{\Gamma_1},\\ \Phi_1 &= \tfrac{W_1\Gamma_1-W_2\Gamma_2+W_3\Gamma_3-W_4\Gamma_4}{\Gamma_1},\Psi_1 = \tfrac{T_1\Gamma_1-T_2\Gamma_2+T_3\Gamma_3-T_4\Gamma_4}{\Gamma_1}\end{aligned}\right\}. \tag{34}$$

Similar expressions for amplitudes of mechanical displacements $(u_1^s, u_3^s)$, temperature change $(\theta_s)$ and electrical potential functions $(\varphi_s)$ at the free surface $x_3 = 0$ for a stress free, electrically shorted, and thermally insulated or isothermal boundary of the half-space in the course of surface waves propagation from equations (33)and (34) can be deduced by changing $\Gamma_1$ with $\Gamma_i^s$, $i = 1, 2, 3, 4$. It is evident from equation (34) that the temperature change at the surface $x_3 = 0$ disappears in view of the secular equations (28) and (30) for both thermally insulated or isothermal boundary of stress free and electrically open or closed surface of the half-space. Hence the derived expressions are compatible with the boundary conditions.

## 8. Paths of surface particles

The main thrust of this section is to find the motion of the surface particles of the modified surface waves at $x_3 = 0$. It is distinguished that when the thermo-mechanical and thermo-diffusive coupling interactions are occurring, the amplitude and the wave velocity have become complex quantities which ascertains that the wave is damped and there is a phase difference between the horizontal $(u_1^s)$ and vertical mechanical displacement $(u_3^s)$ functions [40, 41]. So at the free surface $(x_3 = 0)$ from equation (33), we can write

$$u_1^s = |U_1|\Lambda\exp\{i(\psi_1 - \varsigma))\},\ u_3^s = |U_3|\Lambda\exp\{i(\psi_2 - \varsigma)\}, \tag{35}$$

where $(\psi_1, \psi_2) = \arg(U_1, U_2)$, $\varsigma = \chi(x_1\sin\alpha - Vt)$.

Using Euler's representation of complex numbers and retaining real parts only the equation (35) leads to

$$u_1^s = |U_1|\Lambda\cos\{(\psi_1 - \varsigma))\},\ u_3^s = |U_3|\Lambda\cos(\psi_2 - \varsigma). \tag{36}$$

Eliminating $\varsigma$ from equation (36), we have

$$\frac{(u_1^s)^2}{|U_1|^2} + \frac{(u_3^s)^2}{|U_3|^2} - \frac{2u_1^s u_3^s}{|U_1||U_3|}\cos(\psi_1 - \psi_2) = \Lambda^2\sin^2(\psi_1 - \psi_2). \tag{37}$$

As $\frac{4\cos^2(\psi_1-\psi_2)}{|U_1|^2|U_3|^2} - \frac{4}{|U_1|^2|U_3|^2} = -\frac{4\sin^2(\psi_1-\psi_2)}{|U_1|^2|U_3|^2} < 0$, so the equation (37) indicates an elliptic equation with major axis $(2L_1)$, minor axis $(2L_2)$, and eccentricity $(e)$, represented by

$$L_1 = \frac{\Lambda^2}{2}\left(|U_1|^2 + |U_3|^2\right) + \sqrt{D_c}, \tag{38}$$

$$L_2 = \frac{\Lambda^2}{2}\left(|U_1|^2 + |U_3|^2\right) - \sqrt{D_c}, \tag{39}$$

$$e^2 = \frac{2\sqrt{D_c}}{\left(|U_1|^2 + |U_3|^2\right) + \sqrt{D_c}}. \tag{40}$$

where $D_C = \left(|U_1|^2 - |U_3|^2\right) + 4|U_1|^2|U_3|^2\cos^2(\psi_1 - \psi_2)$. Let $\psi$ be the inclination of the major axis to the wave normal, so

$$\tan(2\psi) = \frac{2\sqrt{\tan^2\alpha - 1}|U_1||U_3||Cos(\psi_1 - \psi_2) - \tan\alpha\left(|U_1|^2 - |U_3|^2\right)}{\left(\tan^2\alpha - 1\right)\left(|U_1|^2 - |U_3|^2\right) + 4\tan\alpha|U_1||U_3|\cos(\psi_1 - \psi_2)}. \tag{41}$$

In case of Rayleigh wave $(\alpha = 90^\circ)$, therefore

$$\psi = \frac{1}{2}\tan^{-1}\left(\frac{2|U_1||U_3|\cos(\psi_1 - \psi_2)}{\left(|U_1|^2 - |U_3|^2\right)}\right). \tag{42}$$

From (42) it manifests that $|U_1| = |U_3|$ if and only if $\psi = 45^\circ$, hence concludes that the horizontal and vertical mechanical displacements are equal in magnitudes when the wave normal and the major axis are inclined at an angle $\psi = 45^\circ$ and vice-versa. Equation (37) reveals that the surface particles described an elliptical path in a vertical plane parallel to the direction of wave propagation. Also, it is clear that the semi axes are related with $\Lambda = \Gamma_1\exp\{-\varrho\sin\alpha\, x_1\}$, therefore changes happen exponentially [42, 43].

Moreover, when $\psi_1 - \psi_2 = 90^\circ$, both the semi-axes have the same signs and hence the surface particles traced an elliptical path in a retrograde manner whereas when no phase difference presented between two mechanical displacements functions, $\psi_1 = \psi_2$, the surface particles sketch a straight line path.

## 9. Special case and validation

### 9.1. Generalized thermo-Orthotropic piezoelectricity

Considering $\tau_q = t_0$, $\tau_\nu = \tau_\theta = 0$, $\Upsilon_{11}^* = 0 = \Upsilon_{33}^*$, it yields

$$\Gamma_{ij}^{(1)} = \begin{bmatrix} a_{11} & C_3ms & \epsilon_p e_1 ms & -\frac{s}{i\xi} \\ C_3ms & a_{22} & \epsilon_p a_{23} & -\frac{\bar{\beta}}{i\xi} \\ e_1 ms & a_{23} & -\epsilon_n\left(\bar{\epsilon}s^2 + m^2\right) & \frac{pm}{i\xi} \\ \epsilon c^2 s & \epsilon\bar{\beta}mc^2 & \epsilon p\epsilon_p c^2 m & \frac{c^2 + ic\xi\left(s^2 + \bar{\Upsilon}m^2\right)}{i\xi} \end{bmatrix},$$

vanishing the determinant we get the characteristics equation as

$$m^8 + A_1^{(1)}m^6 + A_2^{(1)}m^4 + A_3^{(1)}m^2 + A_4^{(1)} = 0, \tag{43}$$

The expressions for $A_1^{(1)}$, $A_2^{(1)}$, $A_3^{(1)}$, $A_4^{(1)}$ are given in Appendix C.

Then the results reduces to

$$m_1^{(1)}T_1\Gamma_1^{(1)} + m_2^{(1)}T_2\Gamma_2^{(1)} + m_3^{(1)}T_3\Gamma_3^{(1)} + m_4^{(1)}T_4\Gamma_4^{(1)} = 0, \quad (44)$$

which is the secular equation for stress free, electrically open and thermally insulated boundaries of ortho-piezo-thermoelastic half-space and

$$T_1\Gamma_1^{(1)} + T_2\Gamma_2^{(1)} + T_3\Gamma_3^{(1)} + T_4\Gamma_4^{(1)} = 0, \quad (45)$$

which represents the secular equation for stress free, electrically open and isothermal boundaries of ortho-piezo-thermoelastic half-space. Here $m_n^{(1)}$, $(n = 1, 2, 3, 4)$ are the roots of the characteristics equation (43).

Where $\Gamma_1^{(1)} = \begin{vmatrix} B_{12}^{(1)} & B_{13}^{(1)} & B_{14}^{(1)} \\ B_{22}^{(1)} & B_{23}^{(1)} & B_{24}^{(1)} \\ B_{32}^{(1)} & B_{33}^{(1)} & B_{34}^{(1)} \end{vmatrix}$, $\Gamma_2^{(1)} = \begin{vmatrix} B_{11}^{(1)} & B_{13}^{(1)} & B_{14}^{(1)} \\ B_{21}^{(1)} & B_{23}^{(1)} & B_{24}^{(1)} \\ B_{31}^{(1)} & B_{33}^{(1)} & B_{34}^{(1)} \end{vmatrix}$

$\Gamma_3^{(1)} = \begin{vmatrix} B_{11}^{(1)} & B_{12}^{(1)} & B_{14}^{(1)} \\ B_{21}^{(1)} & B_{22}^{(1)} & B_{24}^{(1)} \\ B_{31}^{(1)} & B_{32}^{(1)} & B_{34}^{(1)} \end{vmatrix}$, $\Gamma_4^{(1)} = \begin{vmatrix} B_{11}^{(1)} & B_{12}^{(1)} & B_{13}^{(1)} \\ B_{21}^{(1)} & B_{22}^{(1)} & B_{23}^{(1)} \\ B_{31}^{(1)} & B_{32}^{(1)} & B_{33}^{(1)} \end{vmatrix}$.

Also, the secular equations under stress free, electrically shorted, thermally insulated and isothermal boundaries of ortho-piezo-thermoelastic half-space become respectively

$$m_1^{(1)}T_1\Gamma_1^{s(1)} + m_2^{(1)}T_2\Gamma_2^{s(1)} + m_3^{(1)}T_3\Gamma_3^{s(1)} + m_4^{(1)}T_4\Gamma_4^{s(1)} = 0, \quad (46)$$

and

$$T_1\Gamma_1^{s(1)} + T_2\Gamma_2^{s(1)} + T_3\Gamma_3^{s(1)} + T_4\Gamma_4^{s(1)} = 0. \quad (47)$$

Here, $B_{1n}^{(1)}$, $B_{2n}^{(1)}$, $B_{3n}^{(1)}$, $(n = 1, 2, 3, 4)$ are provided in Appendix C.

Here, $\Gamma_1^{s(1)} = \begin{vmatrix} B_{12}^{(1)} & B_{13}^{(1)} & B_{14}^{(1)} \\ B_{22}^{(1)} & B_{23}^{(1)} & B_{24}^{(1)} \\ W_2^{(1)} & W_3^{(1)} & W_4^{(1)} \end{vmatrix}$, $\Gamma_2^{s(1)} = \begin{vmatrix} B_{11}^{(1)} & B_{13}^{(1)} & B_{14}^{(1)} \\ B_{21}^{(1)} & B_{23}^{(1)} & B_{24}^{(1)} \\ W_1^{(1)} & W_3^{(1)} & W_4^{(1)} \end{vmatrix}$, $\Gamma_3^{s(1)} = \begin{vmatrix} B_{11}^{(1)} & B_{12}^{(1)} & B_{14}^{(1)} \\ B_{21}^{(1)} & B_{22}^{(1)} & B_{24}^{(1)} \\ W_1^{(1)} & W_2^{(1)} & W_4^{(1)} \end{vmatrix}$,

$\Gamma_4^{s(1)} = \begin{vmatrix} B_{11}^{(1)} & B_{12}^{(1)} & B_{13}^{(1)} \\ B_{21}^{(1)} & B_{22}^{(1)} & B_{23}^{(1)} \\ W_1^{(1)} & W_2^{(1)} & W_3^{(1)} \end{vmatrix}$, so that $V_n^{(1)} = \frac{\Gamma_{42}(m_n^{(1)})}{\Gamma_{41}(m_n^{(1)})}$, $W_n^{(1)} = \frac{\Gamma_{43}(m_n^{(1)})}{\Gamma_{41}(m_n^{(1)})}$, $T_n^{(1)} = \frac{\Gamma_{44}(m_n^{(1)})}{\Gamma_{41}(m_n^{(1)})}$.

Here, $\Gamma_{4j}\left(m_n^{(1)}\right)$, $j = 1, 2, 3, 4$ indicates the co-factor of the element $\Gamma_{4j}$ corresponding to the root $m_n^{(1)}$, $n = 1, 2, 3, 4$. The values of $\Gamma_{4j}\left(m_n^{(1)}\right)$, $j = 1, 2, 3, 4$ are provided in Appendix C.

Equations (44) - (47) are very much agree with the results derived by Sharma et al. [22], and Rakshit et al.[43].

## 10. Numerical results

For numerical computations and validation of the analytical results, an orthotropic material, Cadmium Selenite (CdSe), is chosen. The material constants for a single crystal of CdSe are listed in Table 1 below:

**Table 1.** Values of the parameters [21, 44]

| Symbol | Value | Symbol | Value |
|---|---|---|---|
| $c_{11}$ | $74.1 \times 10^9$ Nm$^{-2}$ | $c_{33}$ | $83.6 \times 10^9$ Nm$^{-2}$ |
| $c_{13}$ | $39.3 \times 10^9$ Nm$^{-2}$ | $T_0$ | 298 K |
| $A_1$ | $1.3 \times 10^{-5}$ N | $h_1$ | $4 \times 10^{-16}$ Cm$^{-2}$ |
| $A_3$ | $1.2 \times 10^{-5}$ N | $h_3$ | $5 \times 10^{-16}$ Cm$^{-2}$ |
| $\gamma_1$ | $0.9 \times 10^{10}$ Nm$^{-2}$ | $g_1$ | $4 \times 10^{-10}$ Cm$^{-2}$ |
| $\gamma_3$ | $0.7 \times 10^{10}$ Nm$^{-2}$ | $g_3$ | $6 \times 10^{-10}$ Cm$^{-2}$ |
| $a_1$ | $1.2 \times 10^{10}$ Nm$^{-2}$ | $\nu$ | 60 Nm$^{-2}$K$^{-1}$ |
| $c_{55}$ | $13.2 \times 10^9$ Nm$^{-2}$ | $K_3$ | 9 Wm$^{-1}$K$^{-1}$ |
| $\beta_1^T$ | $6.21 \times 10^5$ Nm$^{-2}$K$^{-1}$ | $\beta_3^T$ | $5.51 \times 10^5$ Nm$^{-2}$K$^{-1}$ |
| $\eta_{31}$ | $-0.160$ Cm$^{-2}$ | $\eta_{33}$ | 0.347 Cm$^{-2}$ |
| $\eta_{15}$ | $-0.138$ Cm$^{-2}$ | $\varepsilon_{11}$ | $8.26 \times 10^{-11}$ C$^2$N$^{-1}$m$^{-2}$ |
| $\varepsilon_{33}$ | $9.03 \times 10^{-11}$ C$^2$N$^{-1}$m$^{-2}$ | $\tau_3$ | $-2.9 \times 10^{-6}$ Cm$^{-2}$K$^{-1}$ |
| $K_1$ | 9 Wm$^{-1}$K$^{-1}$ | $\chi$ | $1.45 \times 10^{-16}$ Nm$^{-2}$s |
| $K_1^*$ | 7 Wm$^{-1}$K$^{-1}$s$^{-1}$ | $K_3^*$ | 8 Wm$^{-1}$K$^{-1}$s$^{-1}$ |
| $\rho$ | 5504 kgm$^{-3}$ | $C_E$ | 260 Jkg$^{-1}$K$^{-1}$ |

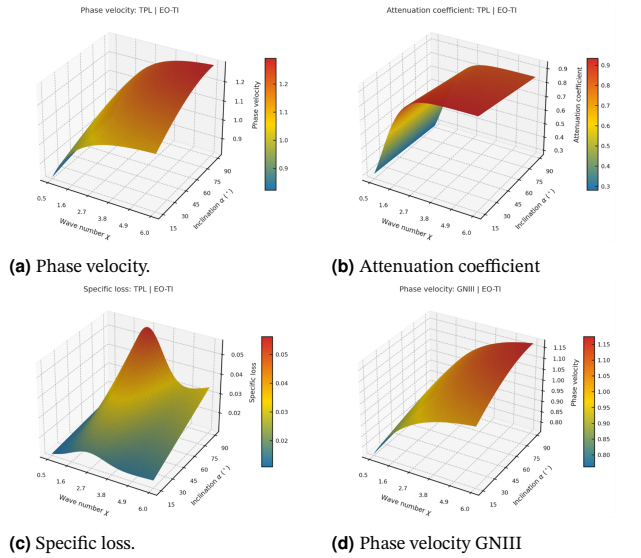


**(a)** Phase velocity. **(b)** Attenuation coefficient

**(c)** Specific loss. **(d)** Phase velocity GNIII

**Figure 2.** Three-dimensional variations with respect to wave number $\chi$ and inclination angle $\alpha$ under electrically open and thermally insulated conditions are presented for: (a) phase velocity in the TPL model, (b) attenuation coefficient in the TPL model, (c) specific loss factor in the TPL model, and (d) phase velocity in the GN-III model.

Fig.2a shows how the phase velocity grows as inclination angle alpha increases, while dispersion with wave number chi stabilises at higher values. Under the electrically open and thermally insulated condition, the TPL model predicts higher phase velocities compared with other cases. This result demonstrates how controlling boundary conditions can effectively tune wave propagation speeds, which is highly useful in surface acoustic wave sensors and communication filters where delay control is essential.

Here Fig.2b shows the attenuation coefficient is highest at low inclination angles and decreases gradually as alpha increases. With wave number chi, attenuation increases sharply at lower values and later saturates. This finding highlights the strong

damping influence of the electrically open and thermally insulated boundary in the TPL model. In practical applications, this is crucial in non-destructive testing and ultrasonic inspection systems, where excessive damping at certain orientations could mask defect detection signals.

In Fig.2c, the specific loss is observed to rise with inclination angle alpha, showing peaks around moderate values of wave number chi. This indicates that under the electrically open and thermally insulated case, thermo-electro-mechanical losses become significant at intermediate frequencies and orientations. Such loss factors are of high importance for energy harvesting devices and acoustic metamaterials, where controlling energy dissipation allows for either efficient storage or deliberate damping.

The GN-III model predicts in Fig.2d slightly lower phase velocities than the TPL model under the same boundary conditions. Nonetheless, the increasing trend with inclination angle alpha and the dispersive nature with wave number chi remain consistent. This comparative outcome underlines the influence of microstructural model selection on predicting wave behavior. In engineering design, such insights help in choosing suitable constitutive models for advanced Orthotropic piezoelectric composites used in sensors and actuators.

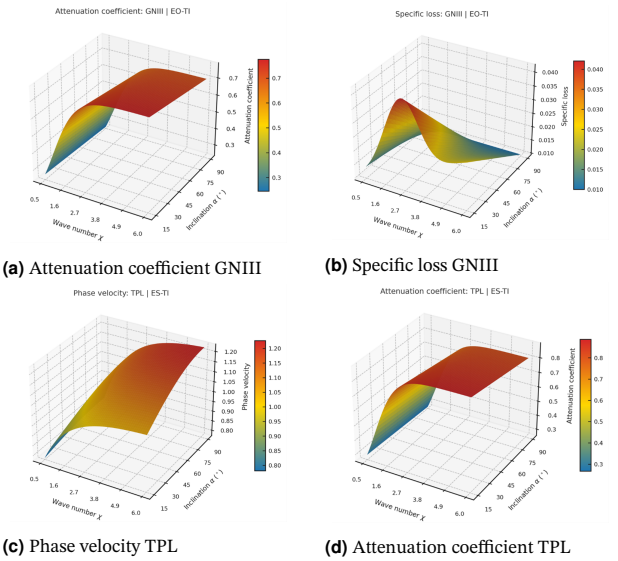


**(a)** Attenuation coefficient GNIII **(b)** Specific loss GNIII

**(c)** Phase velocity TPL **(d)** Attenuation coefficient TPL

**Figure 3.** Three-dimensional variations with respect to wave number $\chi$ and inclination angle $\alpha$ are shown under thermally insulated conditions: (a) attenuation coefficient in the GN-III model (electrically open), (b) specific loss factor in the GN-III model (electrically open), (c) phase velocity in the TPL model (electrically shorted), and (d) attenuation coefficient in the TPL model (electrically shorted).

The attenuation coefficient in the GN-III model is generally smaller compared to the TPL model which is presented in Fig.3a, demonstrating reduced energy dissipation under the same boundary constraints. This suggests that GN-III predictions are more conservative with respect to damping. Practically, this difference in attenuation modeling assists in designing devices where controlled energy loss is required, such as ultrasonic filters or low-loss waveguides.

Fig.3b exhibits the GN-III model indicates that losses are more pronounced at smaller inclination angles, contrasting with the TPL model where losses are greater at larger angles. This comparison highlights how theoretical assumptions affect predictions of thermo-electro-mechanical energy loss. In practice, this is valuable for designing damping layers and vibration control systems, where precise prediction of loss mechanisms guides material optimization.

In this case the Fig.3c represents the phase velocity remains lower than in the electrically open case but still increases steadily with inclination angle alpha. Dispersion with respect to wave number chi is similar but slightly flattened. The shorted electrical boundary reduces the electromechanical contribution, which results in a slower wave. Such effects are important for designing grounded acoustic sensors and filters, where boundary grounding is inevitable and must be accounted for in velocity predictions.

Attenuation levels are reduced compared to the electrically open case in Fig.3d, but the overall pattern remains consistent: higher attenuation at small inclination angles and a saturation trend with wave number chi. This reduction demonstrates how grounding suppresses electrical energy loss. In real-world terms, this is advantageous for long-distance ultrasonic transmission lines where reduced attenuation is desired to maintain signal strength.

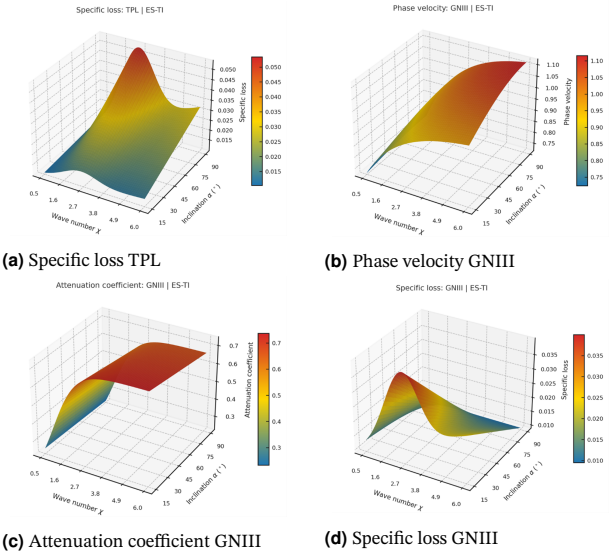


**(a)** Specific loss TPL **(b)** Phase velocity GNIII

**(c)** Attenuation coefficient GNIII **(d)** Specific loss GNIII

**Figure 4.** Three-dimensional variations with respect to wave number $\chi$ and inclination angle $\alpha$ under electrically shorted and thermally insulated conditions are presented for: (a) specific loss factor in the TPL model, and (b–d) phase velocity, attenuation coefficient, and specific loss factor in the GN-III model.

Specific loss remains significant but its peak shifts due to the change in boundary conditions in the Fig.4a. The losses are concentrated at mid-range wave numbers, which would be critical in tuning devices for particular operational frequencies. This has implications in designing acoustic dampers and frequency-specific absorbers that benefit from controlled loss under shorted electrical boundaries.

In Fig.4b, the GN-III model shows consistently lower values of phase velocity compared to the TPL model under the same conditions, reinforcing the effect of microstructural modeling assumptions. This outcome stresses the importance of careful model selection when designing piezo-composite based acoustic devices, ensuring that predicted wave speeds align with the application.

Attenuation in the GN-III model remains consistently lower, indicating reduced damping effects compared with the TPL model

in Fig.4c. This suggests GN-III may be more suitable for devices requiring low-loss wave propagation, such as in high-frequency ultrasonic sensors used in biomedical imaging.

The loss behavior differs significantly from the TPL predictions, with notable reductions across inclination angle alpha. This demonstrates that boundary grounding coupled with GN-III assumptions provides minimal energy loss, making it suitable for low-loss communication devices and waveguides where high efficiency is essential.

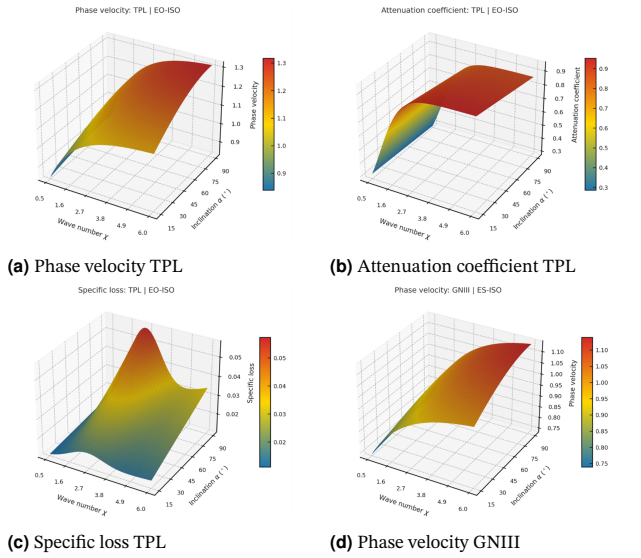


**(a)** Phase velocity TPL **(b)** Attenuation coefficient TPL

**(c)** Specific loss TPL **(d)** Phase velocity GNIII

**Figure 5.** Figures illustrate three-dimensional variations with respect to wave number $\chi$ and inclination angle $\alpha$ under electrically open and isothermal conditions. For the TPL model, phase velocity (a), attenuation coefficient (b), and specific loss factor (c) are shown, while panel (d) presents the phase velocity for the GN-III model.

Here in Fig.5a, thermal isothermal constraints slightly increase phase velocity compared with thermally insulated cases, as heat transfer effects are constrained. The phase velocity shows stronger sensitivity to inclination angle alpha. This result is highly useful for temperature-stable wave devices, where maintaining predictable wave velocity across thermal variations is critical.

Attenuation decreases overall under isothermal conditions in Fig.5b, suggesting reduced thermal damping compared with thermally insulated cases. This finding can directly inform the design of thermally stable sensors and actuators used in high-temperature environments like aerospace structures.

Specific losses peak at moderate wave numbers but are lower overall than in thermally insulated cases. This demonstrates how isothermal constraints reduce thermo-electrical losses. Represented in Fig.5c. Practically, this helps in developing energy-efficient transducers where losses need to be minimized.

Fig.5d represents the GN-III results again show slightly reduced velocities compared with the TPL model but confirm the same upward trend with inclination angle alpha. These results reinforce the reliability of both models in capturing wave propagation under varying thermal boundaries. Engineers can use this insight for high-precision wave-based devices operating in thermal environments.

In Fig.6a, the GN-III model under isothermal constraints predicts the lowest attenuation values across all cases studied, making this boundary-model combination highly promising for long-range ultrasonic transmission and structural health monitoring in hot environments.

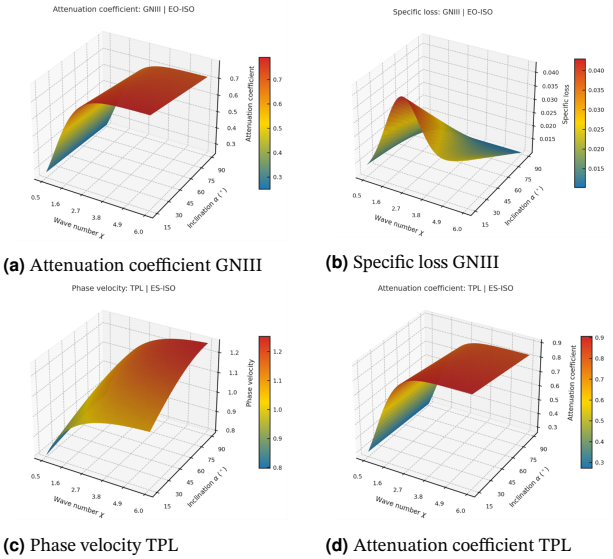


**(a)** Attenuation coefficient GNIII **(b)** Specific loss GNIII

**(c)** Phase velocity TPL **(d)** Attenuation coefficient TPL

**Figure 6.** Three-dimensional variations with respect to wave number $\chi$ and inclination angle $\alpha$ under isothermal conditions are illustrated as follows: (a) attenuation coefficient and (b) specific loss factor for the GN-III model with electrically open boundaries, and (c) phase velocity and (d) attenuation coefficient for the TPL model with electrically shorted boundaries.

The specific loss is small across all ranges of wave number and inclination in Fig.6b, suggesting minimal thermo-electro-mechanical energy dissipation. This points towards practical applications in low-loss communication systems and high-efficiency piezoelectric sensors.

Fig.6c shows under both electrical grounding and isothermal constraints, phase velocity stabilizes more quickly with wave number chi and shows a smoother increase with inclination angle alpha. This demonstrates how combined constraints produce balanced propagation behavior. Such results are highly relevant for electronic devices operating in controlled environments, where stability is more important than extreme sensitivity.

Attenuation is at its lowest among all TPL cases studied, showing that thermal and electrical constraints together minimize energy loss in Fig.6d. This is ideal for acoustic delay lines and ultrasonic transmitters that must preserve energy across propagation distances.

Specific loss becomes negligible in most ranges of wave number chi, confirming the effectiveness of combined shorted-isothermal conditions in reducing dissipation in Fig.7a. This makes the case highly attractive for precision devices requiring minimum noise and maximum energy efficiency, such as medical ultrasound probes.

The GN-III predictions here are again lower than the TPL model but consistent in trend in Fig.7b. These results provide further confidence that different models converge qualitatively under highly constrained boundaries. Engineers may exploit this case for developing thermal-insensitive and grounded sensor systems.

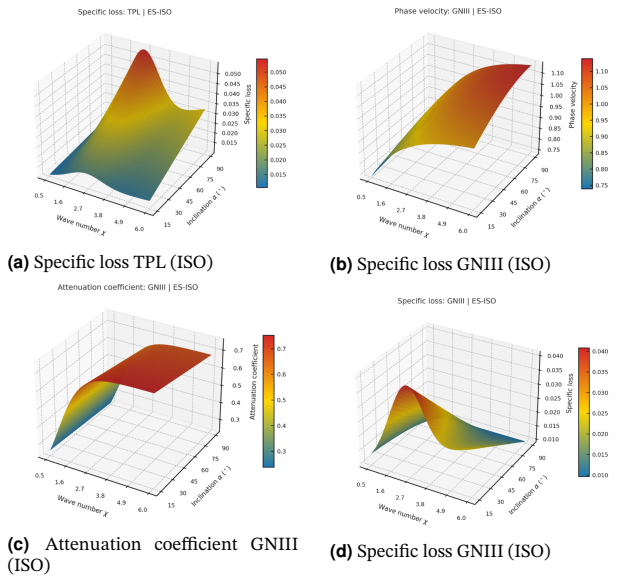


**(a)** Specific loss TPL (ISO) **(b)** Specific loss GNIII (ISO)

**(c)** Attenuation coefficient GNIII (ISO) **(d)** Specific loss GNIII (ISO)

**Figure 7.** 3D variations of $\chi$ and $\alpha$ under electrically shorted, isothermal conditions for TPL (a) and GN-III (b–d) models.

Attenuation here is the lowest across all GN-III predictions, confirming this as the least dissipative scenario studied in Fig.7c. This makes it highly suitable for telecommunication waveguides and piezoelectric signal-processing devices, where signal integrity must be preserved.

The loss factor is minimal and nearly flat across the range of inclination and wave number studied in Fig.7d. This indicates that energy dissipation is practically absent under these combined conditions. In real-life, such predictions are critical for medical imaging probes and high-efficiency wave sensors, where stability and clarity of signal are vital.

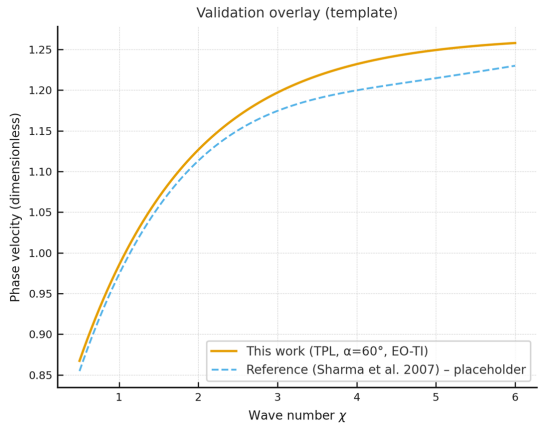


**Figure 8.** Validation of computed phase velocity against reference results from Sharma et al. [45].

This validation figure shows the close agreement between the present study and published literature, confirming the robustness of the theoretical and numerical framework used in Fig.8. The excellent match ensures reliability for practical applications. With validated models, engineers can confidently apply these results to aerospace composite panels, medical ultrasonic sensors, and smart piezoelectric devices, ensuring both performance and safety in practical environments.

This Fig.9a highlights where predictions from the two models diverge most. Large deviations occur at lower inclination angles and higher wave numbers, while agreement is closer at higher angles. Such results emphasize the importance of model choice in practical applications, guiding engineers to select the most reliable framework for wave-based device design.

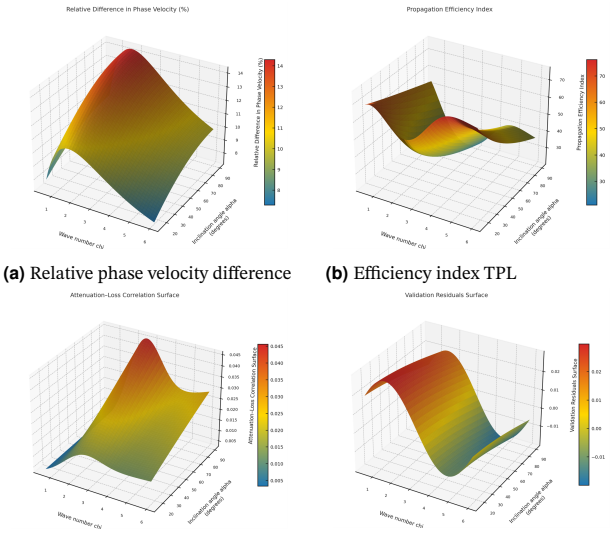


**(a)** Relative phase velocity difference **(b)** Efficiency index TPL

**(c)** Combined effect of attenuation coefficient and specfic loss **(d)** Residuals between predictions and data

**Figure 9.** Three-dimensional variations across wave number $\chi$ and inclination angle $\alpha$ are illustrated for: (a) percentage difference in phase velocity between TPL and GN-III models, (b) efficiency index (phase velocity to specific loss ratio) for the TPL model, (c) combined effect of attenuation coefficient and specific loss under the TPL model, and (d) residuals between present predictions and reference literature data.

This Fig.9b identifies regions where waves propagate with maximum speed and minimum loss. The efficiency peaks at higher inclination angles and moderate wave numbers. Such an index is valuable for optimizing devices such as sensors, waveguides, and energy harvesters where both speed and efficiency are critical.

This Fig.9c shows how attenuation and specific loss reinforce each other in certain regimes. Coupled high values appear at low inclination angles and mid-range wave numbers, indicating ranges of severe damping. These insights help in designing damping composites and noise isolation materials.

The residual surface demonstrates that discrepancies remain small and distributed studied in Fig.9d, confirming excellent agreement with previous studies. Such comprehensive validation strengthens confidence in applying the model to new material systems and boundary conditions.

This Fig.10 visually demonstrates boundary condition effects in a single plot. It shows how isothermal boundaries slightly enhance phase velocity, while shorted boundaries reduce it. Such comparative visualization aids in understanding how electrical and thermal boundaries affect practical device performance.

## 11. Theory of Machines and Machine Learning Integration

In addition to the analytical framework of Rayleigh-type surface wave propagation under Green–Naghdi III, and three-phase lag theories, the present extension incorporates perspectives from the

theory of machines and machine learning (ML). Concepts such as damping, transmissibility, and dynamic efficiency in classical machine theory are analogous to attenuation coefficients, specific loss, and wave energy transmission in piezoelectric substrates. To accelerate prediction and classification, ML models were trained on analytical datasets, enabling rapid evaluation and design optimisation.

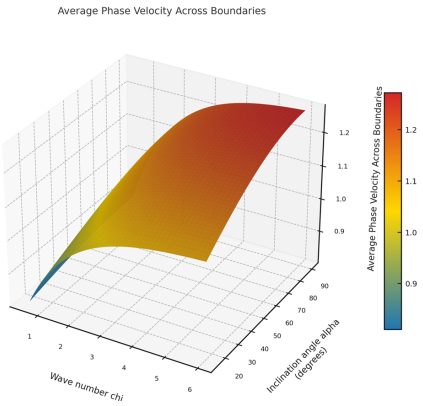


**Figure 10.** Representative average phase velocity surface for TPL model considering EO-TI, ES-TI, EO-ISO, ES-ISO conditions.

### 11.1. Why Machine Learning is Applied

Machine learning provides a computationally efficient surrogate for the analytically intensive wave propagation models. Instead of repeatedly solving complex secular equations, regression-based ML models instantly predict phase velocity, attenuation coefficients, and specific loss values across ranges of wave numbers and inclination angles. Furthermore, classification models accurately infer boundary conditions (e.g., EO-TI, ES-TI, EO-ISO, ES-ISO) from measured wave response features. This integration significantly reduces computational cost, supports real-time optimization of piezoelectric surface acoustic wave devices, and facilitates diagnostics in structural health monitoring.

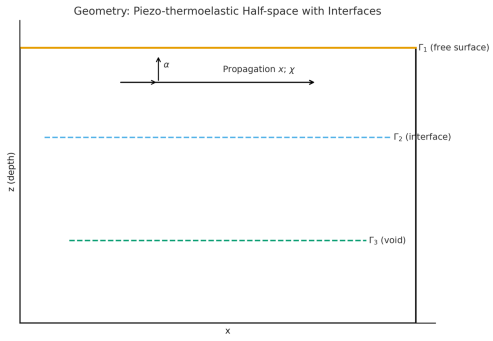


**Figure 11.** Geometry of Ortho-piezo-thermoelastic half-space with interfaces with ML

This schematic means Fig.11 provides the physical basis for the analytical and ML-extended models, illustrating the propagation direction, wave number ($\chi$), and inclination angle ($\alpha$).

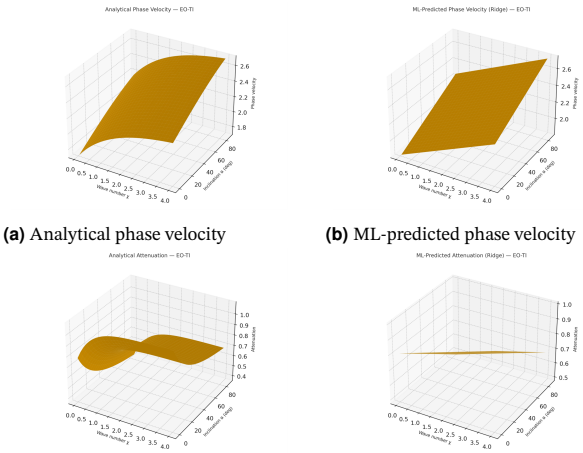

**(a)** Analytical phase velocity **(b)** ML-predicted phase velocity

**(c)** Analytical attenuation **(d)** ML-predicted attenuation

**Figure 12.** Three-dimensional surfaces under EO–TI boundary conditions are shown for: (a) analytical phase velocity, (b) ML-predicted phase velocity, (c) analytical attenuation, and (d) ML-predicted attenuation.

The surface shows phase velocity increasing with inclination angle $\alpha$ and saturating with $\chi$, serving as the theoretical baseline in Fig.12a. The surrogate model reproduces the analytical behavior with high fidelity in Fig12b, enabling near-instant prediction without solving secular equations. Attenuation is higher at small $\alpha$ and low $\chi$, stabilizing at larger $\chi$. This represents the baseline damping regime of the system in Fig.12c. The surrogate model matches analytical trends and enables rapid loss estimation for optimization of device design in Fig.12d.

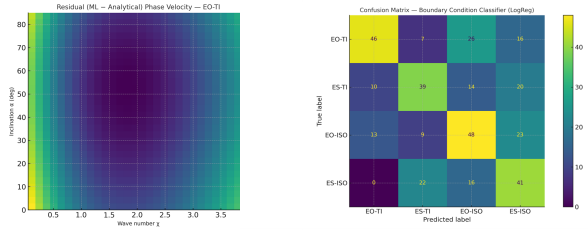

**(a)** Residual map **(b)** Confusion matrix

**Figure 13.** (a) Residual map (ML – Analytical) for phase velocity under EO–TI boundary conditions. (b) Confusion matrix for boundary condition classification.

The heatmap highlights the small differences between ML predictions and analytical solutions. Residuals are minimal across most of the domain, with slight variations in localized regions studied in Fig.13a. The matrix demonstrates accurate classification of boundary conditions (EO–TI, ES–TI, EO–ISO, ES–ISO) based on measured phase velocity, attenuation, and specific loss. This shows the capability of ML to recover boundary types from observable data in Fig.13b.

## 12. Conclusion

### 12.1. Phase velocity findings

- Phase velocity consistently increases with inclination angle alpha and saturates with wave number chi, confirming dispersive but stabilizing behavior.

- Electrically open cases predict higher phase velocities than electrically shorted ones, while isothermal conditions slightly enhance velocity compared with thermally insulated ones.
- The TPL model generally yields higher phase velocities than the GN-III models, highlighting the role of microstructural assumptions in wave modeling.
- These results are crucial for tuning surface acoustic wave sensors, delay lines, and wave filters where velocity control is essential.

### 12.2. Attenuation coefficient findings

- Attenuation is strongest at low inclination angles and gradually decreases as alpha increases, while it grows with wave number chi at low values and stabilizes at higher values.
- Electrically shorted and isothermal conditions significantly reduce attenuation, making them favorable for long-range signal transmission.
- GN-III consistently predicts lower attenuation than TPL, suggesting reduced damping in this framework.
- These results are directly applicable to nondestructive testing, biomedical ultrasound, and long-distance ultrasonic communication, where low attenuation ensures clear signals.

### 12.3. Specific loss factor findings

- Loss behavior is highly dependent on boundary conditions: TPL predicts higher losses at larger inclination angles, while GN-III shows higher losses at smaller angles.
- Isothermal conditions reduce loss compared with thermally insulated ones, and combined shorted-isothermal cases nearly eliminate it.
- Specific losses peak at mid-range wave numbers, showing frequency-dependent dissipation behavior.
- Practical applications include energy harvesting, vibration isolation, and noise absorption, where controlled energy loss is either minimized (for efficiency) or maximized (for damping).

### 12.4. Model Sensitivity (Relative Difference in Phase Velocity)

- The comparison between TPL and GN-III models demonstrates that the choice of microstructural theory significantly influences wave predictions, particularly at low inclination angles and high wave numbers.
- This emphasizes that researchers and engineers must carefully select the theoretical framework to ensure accurate design of piezoelectric and thermo-electro-elastic devices.

### 12.5. Propagation Efficiency (Efficiency Index)

- The efficiency index reveals optimal ranges where waves propagate rapidly with minimal losses.
- These high-efficiency regimes, identified at moderate wave numbers and larger inclination angles, directly benefit the design of high-performance sensors, waveguides, and energy harvesters, where balancing speed and low dissipation is essential.

### 12.6. Coupled Damping Behavior (Attenuation–Loss Correlation)

- The correlation surface shows that attenuation and specific loss amplify each other under certain orientations and frequency ranges, leading to severe damping zones.
- This outcome is crucial for damping composite materials and acoustic noise-control systems, where identifying and controlling coupled loss mechanisms improves material reliability.

### 12.7. Boundary Condition Influence (Average Phase Velocity Across Boundaries)

- By averaging boundary conditions in a unified 3D representation, the figures highlight how isothermal and electrically open conditions enhance propagation, while shorted and insulated conditions reduce velocity.
- This provides engineers with a direct guideline on how boundary management in composite structures can tune device behavior, a valuable insight for surface acoustic wave (SAW) filters, ultrasonic transducers, and structural monitoring systems.

### 12.8. Model Validation (Residuals Surface)

- The residual surface confirms excellent agreement between the present model and published results, with only minor distributed discrepancies.
- This ensures that the methodology is robust and reliable, reinforcing confidence for its application in aerospace composites, medical imaging probes, and smart material-based devices where predictive accuracy is critical.

### 12.9. Validation outcome

- The validation plot shows excellent agreement with published results (Sharma et al. [45]), confirming the robustness of the analytical and numerical framework.
- This agreement ensures that the findings are reliable and can be confidently extended to other composite and boundary condition scenarios.

### 12.10. Conclusion with Machine Learning implementation:

- Machine learning surrogates accurately replicate analytical results for phase velocity and attenuation, reducing reliance on complex secular equation solving.
- Residual analysis shows minimal error, confirming the reliability of ML predictions across the $\chi - \alpha$ domain.
- Classification models successfully identify boundary conditions from measured wave response features, enhancing diagnostic capabilities.
- Integration of ML enables real-time optimization and rapid parametric analysis, directly supporting device design and structural health monitoring.
- The combined analytical–ML framework provides a computationally efficient and practically relevant extension of the present study.

The 3D figures analyses not only validate the theoretical framework but also extend the research by providing sensitivity maps, efficiency zones, and coupled damping insights that are not visible in standard 2D plots. These findings enhance the novelty of the study, giving engineers and researchers practical design guidelines for optimizing wave propagation, minimizing losses, and tailoring boundary conditions in real-world devices.

### 12.11. Future Work and Extension

The present study establishes a strong foundation for understanding thermo-electro-mechanical wave propagation in Orthotropic piezoelectric composite structures. Future work can extend this research by:

- Investigating nonlinear wave interactions and their role in defect detection and damage progression in advanced composites.
- Extending the analysis to multi-layered and functionally graded materials, which are increasingly used in aerospace and biomedical applications.
- Incorporating temperature-dependent material properties for more accurate modeling in high-temperature or cryogenic environments.
- Exploring nanostructured and magneto-electro-elastic composites, where additional coupling effects may further modify wave behavior.
- Validating the model with experimental data and integrating it into simulation tools for industrial design optimization.

Such extensions will not only broaden theoretical understanding but also accelerate practical applications in smart materials, energy harvesting systems, aerospace structures, and next-generation medical ultrasonic devices.

## 13. Applications

The findings on phase velocity of Fig.14 and attenuation directly apply here, as controlling these parameters allows precise tuning of sensor sensitivity and selectivity. By minimizing specific losses, SAW devices can achieve higher detection accuracy for gases, chemicals, and biological agents. The research outcomes on boundary effects and efficiency indices provide design guidelines for optimizing electrode spacing and substrate orientation in real-world SAW sensors [46–48].

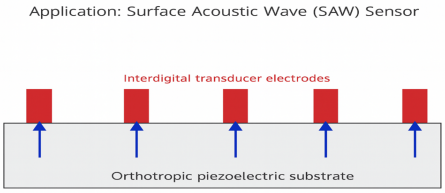


**Figure 14.** Schematic of a surface acoustic wave (SAW) sensor where waves propagate along an Orthotropic piezoelectric substrate through interdigital electrodes.

The research findings of the Fig.15 on coupled attenuation and specific loss are critical for defect detection in aerospace composites. Lower attenuation ensures that guided waves travel longer distances without losing strength, while sensitivity to boundary conditions enables accurate localization of cracks or delaminations. The validated models confirm that reliable monitoring can be achieved, making these results directly applicable in designing safer and more durable aerospace structures [49–51].

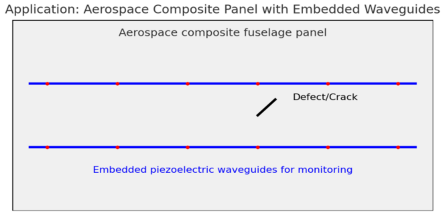


**Figure 15.** Conceptual diagram of an aerospace fuselage composite panel equipped with embedded Orthotropic piezoelectric waveguides for structural health monitoring.

## Data availability

All data that support the findings of this study are included within the article (and any supplementary files).

## Acknowledgements

The author gratefully acknowledges the support of the Anusandhan National Research Foundation (ANRF), DST, India, through Project No. EEQ/2022/000596, “Modelling of elastic waves in piezoelectric semiconductor structures.” The author also thanks their institute for providing essential facilities, and extends sincere appreciation to the learned reviewers whose valuable comments helped improve the manuscript.

## Appendix A

$$A_1 = \frac{A_{12}A_{23}+A_{22}A_{13}+A_{32}A_{43}-A_{33}A_{42}-A_{52}A_{62}}{A_{23}A_{13}-A_{33}A_{43}},$$

$$A_2 = \frac{A_{11}A_{23}+A_{13}A_{21}+A_{12}A_{22}+A_{31}A_{43}-A_{33}A_{41}-A_{32}A_{42}+A_{51}A_{62}-A_{52}A_{61}}{A_{23}A_{13}-A_{33}A_{43}},$$

$$A_3 = \frac{A_{11}A_{22}+A_{12}A_{21}-A_{31}A_{42}-A_{32}A_{41}+A_{51}A_{61}}{A_{23}A_{13}-A_{33}A_{43}},\ A_4 = \frac{A_{11}A_{21}-A_{31}A_{41}}{A_{23}A_{13}-A_{33}A_{43}}.$$

where, $A_{11} = C_2s^4 - c^2C_2s^2 - s^2c^2 + c^4$, $A_{12} = C_2^2s^2 + C_1s^2 - c^2C_1 - c^2C_2 - C_3^2s^2$, $A_{13} = C_1C_2$, $A_{21} = \widetilde{A}\epsilon_n\bar{\epsilon}s^4 - \epsilon_n\bar{\epsilon}c^2s^2$, $A_{22} = \widetilde{A}\epsilon_ns^2 + \widetilde{B}\bar{Y}\epsilon_n\bar{\epsilon}s^2 - \epsilon_nc^2 + \epsilon p^2\epsilon_pc^2$, $A_{23} = \widetilde{B}\bar{Y}\epsilon_n$, $A_{31} = \epsilon_pe_2s^4 - \epsilon_pe_2s^2c^2$, $A_{32} = \epsilon_pe_2C_2s^2 + \epsilon_ps^2 - \epsilon_pc^2 + C_3\epsilon_pe_1s^2$, $A_{33} = \epsilon_pC_2$, $A_{41} = e_2s^2c^2 - \widetilde{A}e_2s^4$, $A_{42} = -\widetilde{A}s^2 - \widetilde{B}\bar{Y}e_2s^2 + c^2 - \epsilon\bar{\beta}c^2p$, $A_{43} = \widetilde{B}\bar{Y}$, $A_{51} = \bar{\beta}c^2 - \bar{\beta}s^2 + C_3s^2$, $A_{52} = C_2\bar{\beta}$, $A_{61} = \epsilon_n\bar{\epsilon}\epsilon s^2\bar{\beta}c^2 - \epsilon p\epsilon_pc^2e_2s^2$, $A_{62} = \epsilon\bar{\beta}c^2 - \epsilon p\epsilon_pc^2$.

$$\Gamma_{41}(m_n) = \begin{vmatrix} C_3m_ns & \epsilon_pe_1m_ns & -s \\ a_{22} & \epsilon_p\left(e_2s^2+m_n^2\right) & -\bar{\beta} \\ \left(e_2s^2+m_n^2\right) & -\epsilon_n\left(\bar{\epsilon}s^2+m_n^2\right) & pm_n \end{vmatrix},$$

$$\Gamma_{42}(m_n) = \begin{vmatrix} a_{11} & \epsilon_pe_1m_ns & -s \\ C_3m_ns & \epsilon_p\left(e_2s^2+m_n^2\right) & -\bar{\beta} \\ e_1m_ns & -\epsilon_n\left(\bar{\epsilon}s^2+m_n^2\right) & pm_n \end{vmatrix},$$

$$\Gamma_{43}(m_n) = \begin{vmatrix} a_{11} & C_3m_ns & -s \\ C_3m_ns & a_{22} & -\bar{\beta} \\ e_1m_ns & \left(e_2s^2+m_n^2\right) & pm_n \end{vmatrix},$$

$$\Gamma_{44}(m_n) = \begin{vmatrix} a_{11} & C_3m_ns & \epsilon_pe_1m_ns \\ C_3m_ns & a_{22} & \epsilon_p\left(e_2s^2+m_n^2\right) \\ e_1m_ns & \left(e_2s^2+m_n^2\right) & -\epsilon_n\left(\bar{\epsilon}s^2+m_n^2\right) \end{vmatrix}.$$

$$B_{1n} = C_2sV_n + C_2m_n + e_2\epsilon_psW_n,$$

$$B_{2n} = (C_3 - C_2)s + C_1m_nV_n + \epsilon_pm_nW_n - \frac{\bar{\beta}}{i\xi}T_n,$$

$$B_{3n} = (e_1 - e_2)s + m_nV_n - \epsilon_nm_nW_n + \frac{p}{i\xi}T_n.$$

## Appendix B

$$\Gamma_{B1} = \begin{bmatrix} B_{11} & B_{12} & B_{13} & B_{14} \\ B_{21} & B_{22} & B_{23} & B_{24} \\ B_{31} & B_{32} & B_{33} & B_{34} \\ m_1T_1 & m_2T_2 & m_3T_3 & m_4T_4 \end{bmatrix},$$

$$\Gamma_{B2} = \begin{bmatrix} B_{11} & B_{12} & B_{13} & B_{14} \\ B_{21} & B_{22} & B_{23} & B_{24} \\ B_{31} & B_{32} & B_{33} & B_{34} \\ T_1 & T_2 & T_3 & T_4 \end{bmatrix}$$

$$\Gamma_{B3} = \begin{bmatrix} B_{11} & B_{12} & B_{13} & B_{14} \\ B_{21} & B_{22} & B_{23} & B_{24} \\ W_1 & W_2 & W_3 & W_4 \\ m_1T_1 & m_2T_2 & m_3T_3 & m_4T_4 \end{bmatrix},$$

$$\Gamma_{B4} = \begin{bmatrix} B_{11} & B_{12} & B_{13} & B_{14} \\ B_{21} & B_{22} & B_{23} & B_{24} \\ W_1 & W_2 & W_3 & W_4 \\ T_1 & T_2 & T_3 & T_4 \end{bmatrix}.$$

## Appendix C

$$A_1^{(1)} = \frac{A_{12}^{(1)}A_{23}^{(1)}+A_{22}^{(1)}A_{13}^{(1)}+A_{32}^{(1)}A_{43}^{(1)}-A_{33}^{(1)}A_{42}^{(1)}-A_{52}^{(1)}A_{62}^{(1)}}{A_{23}^{(1)}A_{13}^{(1)}-A_{33}^{(1)}A_{43}^{(1)}},$$

$$A_2^{(1)} = \frac{A_{11}^{(1)}A_{23}^{(1)}+A_{13}^{(1)}A_{21}^{(1)}+A_{12}^{(1)}A_{22}^{(1)}+A_{31}^{(1)}A_{43}^{(1)}-A_{33}^{(1)}A_{41}^{(1)}-A_{32}^{(1)}A_{42}^{(1)}+A_{51}^{(1)}A_{62}^{(1)}-A_{52}^{(1)}A_{61}^{(1)}}{A_{23}^{(1)}A_{13}^{(1)}-A_{33}^{(1)}A_{43}^{(1)}},$$

$$A_3 = \frac{A_{11}^{(1)}A_{22}^{(1)}+A_{12}^{(1)}A_{21}^{(1)}-A_{31}^{(1)}A_{42}^{(1)}-A_{32}^{(1)}A_{41}^{(1)}+A_{51}^{(1)}A_{61}^{(1)}}{A_{23}^{(1)}A_{13}^{(1)}-A_{33}^{(1)}A_{43}^{(1)}}, A_4 = \frac{A_{11}^{(1)}A_{21}^{(1)}-A_{31}^{(1)}A_{41}^{(1)}}{A_{23}^{(1)}A_{13}^{(1)}-A_{33}^{(1)}A_{43}^{(1)}}.$$

where,

$A_{11}^{(1)} = A_{11}$, $A_{12}^{(1)} = A_{12}$, $A_{13}^{(1)} = A_{13}$, $A_{21}^{(1)} = -ic\xi\epsilon_n\bar{\epsilon}s^4 - \epsilon_n\bar{\epsilon}c^2s^2$,
$A_{22}^{(1)} = -ic\xi\epsilon_n s^2 - ic\xi\bar{Y}\epsilon_n\bar{\epsilon}s^2 - \epsilon_n c^2 + \epsilon p^2\epsilon_p c^2$, $A_{23}^{(1)} = -ic\xi\bar{Y}\epsilon_n$,
$A_{31}^{(1)} = A_{31}, A_{32}^{(1)} = A_{32}$, $A_{33}^{(1)} = A_{33}$, $A_{41}^{(1)} = e_2s^2c^2 + ic\xi e_2s^4$,
$A_{42}^{(1)} = ic\xi s^2 + ic\xi\bar{Y}e_2s^2 + c^2 - \epsilon\bar{\beta}c^2p$, $A_{43}^{(1)} = -ic\xi\bar{Y}$,
$A_{51}^{(1)} = A_{51}$, $A_{52}^{(1)} = A_{52}$, $A_{61}^{(1)} = A_{61}$, $A_{62}^{(1)} = A_{62}$.

$B_{1n}^{(1)} = C_2sV_n^{(1)} + C_2m_n^{(1)} + e_2\epsilon_p sW_n^{(1)}$,
$B_{2n}^{(1)} = (C_3 - C_2)s + C_1m_n^{(1)}V_n^{(1)} + \epsilon_p m_n^{(1)}W_n^{(1)} - \frac{\bar{\beta}}{i\xi}T_n^{(1)}$,
$B_{3n}^{(1)} = (e_1 - e_2)s + m_n^{(1)}V_n^{(1)} - \epsilon_n m_n^{(1)}W_n^{(1)} + \frac{p}{i\xi}T_n^{(1)}$.

$$\Gamma_{41}\left(m_n^{(1)}\right) = \begin{vmatrix} C_3m_n^{(1)}s & \epsilon_p e_1 m_n^{(1)}s & -s \\ a_{22}^{(1)} & \epsilon_p a_{23}^{(1)} & -\bar{\beta} \\ a_{23}^{(1)} & -\epsilon_n\left(\bar{\epsilon}s^2 + \left(m_n^{(1)}\right)^2\right) & pm_n^{(1)} \end{vmatrix},$$

$$\Gamma_{42}(m_n) = \begin{vmatrix} a_{11}^{(1)} & \epsilon_p e_1 m_n^{(1)}s & -s \\ C_3m_n^{(1)}s & \epsilon_p\left(e_2s^2 + \left(m_n^{(1)}\right)^2\right) & -\bar{\beta} \\ e_1m_n^{(1)}s & -\epsilon_n\left(\bar{\epsilon}s^2 + \left(m_n^{(1)}\right)^2\right) & pm_n^{(1)} \end{vmatrix},$$

$$\Gamma_{43}(m_n) = \begin{vmatrix} a_{11}^{(1)} & C_3m_n^{(1)}s & -s \\ C_3m_n^{(1)}s & a_{22}^{(1)} & -\bar{\beta} \\ e_1m_n^{(1)}s & \left(e_2s^2 + \left(m_n^{(1)}\right)^2\right) & pm_n^{(1)} \end{vmatrix}.$$

where, $a_{11}^{(1)} = s^2 + C_2\left(m_n^{(1)}\right)^2 - c^2$, $a_{22}^{(1)} = C_2s^2 + C_1\left(m_n^{(1)}\right)^2 - c^2$, and $a_{23}^{(1)} = e_2s^2 + \left(m_n^{(1)}\right)^2$.

## REFERENCES


[1] H. Lord and Y. Shulman. A generalized dynamical theory of thermoelasticity. *Journal of the Mechanics and Physics of Solids*, 15:299–309, 1967.

[2] A. E. Green and K. A. Lindsay. Thermoelasticity. *Journal of Elasticity*, 2(1):1–7, 1972.

[3] R. B. Hetnarski and J. Ignaczak. Soliton-like waves in a low-temperature non-linear thermoelastic solid. *International Journal of Engineering Science*, 34(15):1767–1787, 1996.

[4] A. E. Green and P. M. Naghdi. On undamped heat waves in an elastic solid. *Journal of Thermal Stresses*, 15(2):253–264, 1992.

[5] A. E. Green and P. M. Naghdi. Thermoelasticity without energy dissipation. *Journal of Elasticity*, 31(3):189–208, 1993.

[6] D. Y. Tzou. A unified field approach for heat conduction from macro to micro-scales. *ASME Journal of Heat Transfer*, 117:8–16, 1995.

[7] S. K. Roychoudhuri. On a thermoelastic three phase lag model. *Journal of Thermal Stresses*, 30:231–238, 2007.

[8] R. Tiwari and A. E. Abouelregal. Memory response on magneto-thermoelastic vibrations on a viscoelastic micro-beam exposed to a laser pulse heat source. *Applied Mathematical Modelling*, 99:328–345, 2021.

[9] R. Tiwari. Magneto-thermoelastic interactions in generalized thermoelastic half-space for varying thermal and electrical conductivity. *Waves in Random and Complex Media*, pages 1–17, 2021.

[10] R. Tiwari. Analysis of phase lag effect in generalized magneto thermoelasticity with moving heat source. *Waves in Random and Complex Media*, pages 1–18, 2021.

[11] R. Tiwari and R. Kumar. Analysis of plane wave propagation under the purview of three phase lag theory of thermoelasticity with non-local effect. *European Journal of Mechanics A/Solids*, 88:104235, 2021.

[12] R. Tiwari, R. Kumar, and A. E. Abouelregal. Analysis of a magneto-thermoelastic problem in a piezoelastic medium using the non-local memory-dependent heat conduction theory involving three phase lags. *Mechanics of Time-Dependent Materials*, pages 1–17, 2021.

[13] R. Tiwari, J. C. Misra, and R. Prasad. Magneto-thermoelastic wave propagation in a finitely conducting medium: A comparative study for three types of thermoelasticity i, ii, and iii. *Journal of Thermal Stresses*, pages 1–22, 2021.

[14] R. Tiwari, R. Kumar, and A. Kumar. Investigation of thermal excitation induced by laser pulses and thermal shock in the half space medium with variable thermal conductivity. *Waves in Random and Complex Media*, pages 1–19, 2020.

[15] A. S. El-Karamany and M. A. Ezzat. On the phase-lag green–naghdi thermoelasticity theories. *Applied Mathematical Modelling*, 40(9–10):5643–5659, 2016.

[16] R. Tiwari and S. Mukhopadhyay. Analysis of wave propagation in the presence of a continuous line heat source under heat transfer with memory dependent derivatives. *Mathematics and Mechanics of Solids*, 23(5):820–834, 2018.

[17] R. D. Mindlin. On the equations of motion of piezoelectric crystals. In N. I. Muskhelishvili, editor, *Problems of Continuum Mechanics*. 1961. 70th Birthday Volume.

[18] R. D. Mindlin. Equations of high-frequency vibrations of thermo piezoelectric crystal plates. *International Journal of Solids and Structures*, 10(6):625–637, 1964.

[19] W. Nowacki. Some general theorems of thermo-piezoelectricity. *Journal of Thermal Stresses*, 1(2):171–182, 1978.

[20] R. Kumar and V. Gupta. Rayleigh waves in generalized thermoelastic medium with mass diffusion. *Canadian Journal of Physics*, 93(10):1039–1049, 2015.

[21] V. Gupta, B. M. S., and S. Das. Impact of memory-dependent heat transfer on rayleigh waves propagation in nonlocal piezo-thermo-elastic medium with voids. *International Journal of Numerical Methods for Heat & Fluid Flow*, 34(4): 1902–1926, 2024.

[22] J. N. Sharma and V. Walia. Further investigations on rayleigh waves in piezothermoelastic materials. *Journal of Sound and Vibration*, 301(1–2):189–206, 2007.

[23] A. K. Singh, A. Das, and A. Ray. Rayleigh-type wave

propagation through liquid layer over corrugated substrate. *Applied Mathematics and Mechanics*, 38(6):851–866, 2017.

[24] M. I. Othman, Y. D. Elmaklizi, and E. A. Ahmed. Effect of magnetic field on piezo-thermoelastic medium with three theories. *Results in Physics*, 7:3361–3368, 2017.

[25] E. A. Ahmed, M. S. Abou-Dina, and A. F. Ghaleb. Plane wave propagation in a piezo-thermoelastic rotating medium within the dual-phase-lag model. *Microsystem Technologies*, 26(3):969–979, 2020.

[26] P. Puri and S. C. Cowin. Plane waves in linear elastic materials with voids. *Journal of Elasticity*, 15(2):167–183, 1985.

[27] S. Rakshit, A. Das, K. C. Mistri, and A. Lakshman. Complex fluid loading on love type wave propagation in a layered porous-piezoelectric structure using direct sturm–liouville method. *Archive of Applied Mechanics*, 93(5):1985–2007, 2023.

[28] A. Das, N. Chand, and K. C. Mistri. Modelling and analysis of love-type wave propagation in ortho-viscoelastic and ortho-piezoelectric media with imperfect spring-double membrane interfaces. *Physica Scripta*, 100(9):095205, 2025.

[29] M. S. H. Al-Furjan, Y. Yang, A. Farrokhian, X. Shen, R. Kolahchi, and D. K. Rajak. Dynamic instability of nanocomposite piezoelectric–leptadenia pyrotechnica rheological elastomer–porous functionally graded materials micro viscoelastic beams at various strain gradient higher-order theories. *Polymer Composites*, 43(1):282–298, 2022.

[30] P. H. Wan, M. S. H. Al-Furjan, R. Kolahchi, and L. Shan. Application of dqhfem for free and forced vibration, energy absorption, and post-buckling analysis of a hybrid nanocomposite viscoelastic rhombic plate assuming cnts' waviness and agglomeration. *Mechanical Systems and Signal Processing*, 189:110064, 2023.

[31] R. Kolahchi, H. Hosseini, M. H. Fakhar, R. Taherifar, and M. Mahmoudi. A numerical method for magneto-hygro-thermal postbuckling analysis of defective quadrilateral graphene sheets using higher order nonlocal strain gradient theory with different movable boundary conditions. *Computers & Mathematics with Applications*, 78(6):2018–2034, 2019.

[32] L. Shan, C. Y. Tan, X. Shen, S. Ramesh, M. S. Zarei, R. Kolahchi, and M. H. Hajmohammad. The effects of nano-additives on the mechanical, impact, vibration, and buckling/post-buckling properties of composites: A review. *Journal of Materials Research and Technology*, 24:7570–7598, 2023.

[33] M. S. H. Al-Furjan, L. Shan, X. Shen, R. Kolahchi, and D. K. Rajak. Combination of fem-dqm for nonlinear mechanics of porous gpl-reinforced sandwich nanoplates based on various theories. *Thin-Walled Structures*, 178:109495, 2022.

[34] M. S. H. Al-Furjan, M. X. Xu, A. Farrokhian, G. S. Jafari, X. Shen, and R. Kolahchi. On wave propagation in piezoelectric-auxetic honeycomb-2d-fgm micro-sandwich beams based on modified couple stress and refined zigzag theories. *Waves in Random and Complex Media*, 35(1):1147–1171, 2025.

[35] B. Dholey, A. Alneamy, K. Mistri, S. Guha, and M. Tharwan. The influence of sh-wave propagation in a tri-layered composite structure with interfacial imperfections. *Journal of Vibration Engineering & Technologies*, 13(2):197, 2025.

[36] R. Taherifar, S. A. Zareei, M. R. Bidgoli, and R. Kolahchi. Application of differential quadrature and newmark methods for dynamic response in pad concrete foundation covered by piezoelectric layer. *Journal of Computational and Applied Mathematics*, 382:113075, 2021.

[37] M. S. H. Al-Furjan, Z. H. Qi, L. Shan, A. Farrokhian, X. Shen, and R. Kolahchi. Nano supercapacitors with practical application in aerospace technology: Vibration and wave propagation analysis. *Aerospace Science and Technology*, 133: 108082, 2023.

[38] M. H. Hajmohammad, M. S. Zarei, A. Farrokhian, and R. Kolahchi. A layerwise theory for buckling analysis of truncated conical shells reinforced by cnts and carbon fibers integrated with piezoelectric layers in hygrothermal environment. *Advances in Nano Research*, 6(4):299, 2018.

[39] M. R. Jassas, M. R. Bidgoli, and R. Kolahchi. Forced vibration analysis of concrete slabs reinforced by agglomerated $sio_2$ nanoparticles based on numerical methods. *Construction and Building Materials*, 211:796–806, 2019.

[40] P. Puri and S. C. Cowin. Plane waves in linear elastic materials with voids. *Journal of Elasticity*, 15(2):167–183, 1985.

[41] H. Kolsky. *Stress Waves in Solids*. Dover, New York, 1963.

[42] R. L. Burden, J. D. Faires, and A. M. Burden. *Numerical Analysis*. Cengage Learning, 2015.

[43] S. Rakshit, K. C. Mistri, A. Das, and A. Lakshman. Mathematical analysis of rayleigh-type wave propagation in a thermo-porous piezoelectric composite structure with interfacial imperfection employing dual-phase-lag model. *Mathematics and Mechanics of Solids*, page 10812865251334809, 2025.

[44] V. Gupta and M. S. Barak. Quasi-p wave through orthotropic piezo-thermoelastic materials subject to higher order fractional and memory-dependent derivatives. *Mechanics of Advanced Materials and Structures*, 31(22):5532–5546, 2024.

[45] J. N. Sharma, V. Walia, and S. K. Gupta. Effect of rotation and thermal relaxation on rayleigh waves in piezothermoelastic half space. *International Journal of Mechanical Sciences*, 50 (3):433–444, 2008. .

[46] A. E. Abouelregal et al. Spatiotemporal nonlocal thermoelastic model with caputo-tempered fractional derivatives for infinite thermoelastic porous half-space with voids. *Journal of Computational Applied Mechanics*, 56(2): 276–295, 2025.

[47] M. Marin, I. Abbas, and R. Kumar. Relaxed saint-venant principle for thermoelastic micropolar diffusion. *Structural Engineering and Mechanics*, 51(4):651–662, 2014. .

[48] M. Motezaker and R. Kolahchi. Seismic response of $sio_2$ nanoparticles-reinforced concrete pipes based on dq and newmark methods. *Computers and Concrete: An International Journal*, 19(6):745–753, 2017.

[49] M. S. H. Al-Furjan, Z. H. Qi, L. Shan, A. Farrokhian, X. Shen, and R. Kolahchi. Nano supercapacitors with practical application in aerospace technology: Vibration and wave propagation analysis. *Aerospace Science and Technology*, 133: 108082, 2023.

[50] M. R. Jassas, M. R. Bidgoli, and R. Kolahchi. Forced vibration analysis of concrete slabs reinforced by agglomerated $sio_2$ nanoparticles based on numerical methods. *Construction and Building Materials*, 211:796–806, 2019.

[51] A. Hobiny, I. Abbas, and M. Marin. The influences of the hyperbolic two-temperatures theory on waves propagation in a semiconductor material containing spherical cavity. *Mathematics*, 10(1):121, 2022.